UCLA
UCLA Electronic Theses and Dissertations

Title
Debris Rings from Extrasolar Irregular Satellites

Permalink
https://escholarship.org/uc/item/95b2x2df

Author
Hayakawa, Kevin

Publication Date
2022

Peer reviewed|Thesis/dissertation

eScholarship.org Powered by the California Digital Library
University of California

UNIVERSITY OF CALIFORNIA

Los Angeles

Debris Rings from Extrasolar Irregular Satellites

A dissertation submitted in partial satisfaction

of the requirements for the degree

Doctor of Philosophy in Astronomy and Astrophysics

by

Kevin T. Hayakawa

2022

© Copyright by
Kevin T. Hayakawa
2022

ABSTRACT OF THE DISSERTATION

Debris Rings from Extrasolar Irregular Satellites

by

Kevin T. Hayakawa
Doctor of Philosophy in Astronomy and Astrophysics
University of California, Los Angeles, 2022
Professor Bradley M. Hansen, Chair

Irregular satellites are the minor bodies found orbiting all four Solar System giant planets, with large semimajor axes, eccentricities, and inclinations. Previous studies have determined that the Solar System's irregular satellites are extremely collisionally evolved populations today, having lost ~99 per cent of their initial mass over the course of hundreds of Myr. Such an evolution implies that the irregular satellites must have produced a population of dusty collisional debris in the past, which is potentially observable due to the resulting reprocessing of stellar light. In this dissertation we examine the signatures of the debris discs produced by extrasolar analogues of this process. Radiation pressure, quantified by the parameter β, is the driving mechanism behind the liberation of dust grains from the planetary Hill sphere, and results in the formation of circumstellar dust rings, even in the absence of an underlying belt of asteroids in the system. Our simulated discs reproduce many of the same features seen in some classes of observed debris discs, such as thin ring morphology, a large blowout size, and azimuthal symmetry. We compare our simulated discs' radial profiles to those of the narrow dust rings observed around Fomalhaut and HR 4796A, and show that they can broadly reproduce the observed radial distribution of dust.

The dissertation of Kevin T. Hayakawa is approved.

Hilke E. Schlichting

Smadar Naoz

Michael P. Fitzgerald

Bradley M. Hansen, Committee Chair

University of California, Los Angeles

2022

To my parents

TABLE OF CONTENTS

LIST OF FIGURES

LIST OF TABLES

ACKNOWLEDGMENTS

First and foremost, I would like to thank my parents Lane and Judy for supporting me as a person and all the decisions I have made until this point. I would also like to thank Darren, Alyssa, and Yukon for all of the memories. Thank you to Uncle Shig, Aunty Wendy, Colin, and Dr. Keri Hayakawa, for inspiring me and showing me that obtaining a Ph.D. was possible in our family. And thank you to my Bachan, Jichan, and Popo.

Thank you to my advisor, Brad, the most patient and optimistic person I have met on my academic journey. Thank you to my thesis committee members, Hilke, Mike, and Smadar. I feel very fortunate that I was able to take at least one course with each of you before assembling my committee. I would also like to thank Yasuhiro Hasegawa, my internship mentor, for providing me with invaluable research and networking opportunities. Thank you to my fellow graduate students, especially my cohort—Adam, Bao Minh, Jon, Jordan, Mathew, and Zhuo—for the late night and weekend study groups. Thank you to my roommates over the years, especially Alec, Jareni, and Yeou, for dealing with me. Thank you to my knitting club members Kevin, Paul, and Shawn for helping me get through a very lonely pandemic.

Chapters 1-6 and 8 have been submitted to the Monthly Notices of the Royal Astronomical Society for publication as a paper entitled ‘Debris Rings from Extrasolar Irregular Satellites’ with Bradley M. Hansen as the sole co-author and PI.

This research has made use of NASA’s Astrophysics Data System. This research was supported by NASA Grant 443820-HN-21577.

VITA

2014	Grader/Reader, Departments of Physics and Astronomy, University of California, Berkeley.
2014–2015	Planetarium Presenter, Lawrence Hall of Science, Berkeley, CA.
2015–2016	Undergraduate Student Instructor, Departments of Physics and Astronomy, University of California, Berkeley.
2016	B.A. (Physics) and B.A. (Astrophysics), University of California, Berkeley.
2016–2017	Teaching Assistant, Department of Physics and Astronomy, UCLA.
2017–2019	Teaching Associate, Department of Physics and Astronomy, UCLA.
2018	M.S. (Astronomy), UCLA, Los Angeles, California.
2019	Adjunct Professor of Astronomy, El Camino College, Torrance, CA.
2020	Adjunct Professor of Astronomy, Santa Monica College, Santa Monica, CA.
2020	Teaching Fellow, Department of Physics and Astronomy, UCLA.
2020-2021	Adjunct Professor of Physics, Moorpark College, Moorpark, CA.
2020–present	Graduate Student Researcher, Department of Physics and Astronomy, UCLA.

PUBLICATIONS

Debris Rings from Extrasolar Irregular Satellites, Kevin T. Hayakawa & Brad Hansen, Monthly Notices of the Royal Astronomical Society (submitted March 2022).

The Lick Observatory Supernova Search follow-up program: *photometry data release of* 70 *stripped-envelope supernovae*, WeiKang Zheng, Benjamin E. Stahl, Thomas de Jaeger, ... , Kevin T. Hayakawa, ... Monthly Notices of the Royal Astronomical Society (2022).

The Berkeley sample of Type II supernovae: *BV RI light curves and spectroscopy of* 55 *SNe II*, T. de Jaeger, W. Zheng, B. E. Stahl, ... , K. T. Hayakawa, ... Monthly Notices of the Royal Astronomical Society (2019).

Lick Observatory Supernova Search Follow-Up Program: *Photometry Data Release of* 93 *Type Ia Supernovae*, Benjamin E. Stahl, WeiKang Zheng, Thomas de Jaeger, ... , Kevin T. Hayakawa, ... Monthly Notices of the Royal Astronomical Society (2019).

CHAPTER 1

Introduction

Planet formation is a dynamic process, wherein the growth of planets is accomplished via a prolonged history of interactions between smaller bodies, leading to scattering and collision (e.g., Lissauer 1993). This process is particularly important during the latter stages of planetary assembly, as planetary systems settle down into their final configurations. Indeed, the process of dynamical clearing is thought to continue for some time after planets have reached their final masses, as the remnants of the source population are ground down and removed from the system (e.g., Goldreich et al. 2004). Stars in this stage of development often show evidence for extended, tenuous, populations of dust (Wyatt 2008). These dust grains scatter and re-radiate light from the central star, and can be observed either by looking for infrared excesses or by imaging in scattered light. The lifetime of dust in such systems is short, limited by radiation pressure and Poynting-Robertson drag (e.g., Burns et al. 1979), but the observation of this material offers essential insights into the architectures of newly formed planetary systems.

As a result, there have been substantial efforts to image such debris systems directly (see Hughes et al. 2018, for a recent summary). The results show a wide range of morphologies, from extended discs (e.g. those around τ Ceti and HD 141569) to very narrow rings, such as those around the stars Fomalhaut, HR 4796A, and HD 141011. The variation in appearance presumably indicates some complexity in the evolution and outcome of the planetary assembly process, and there exist detailed models for the kinds of outcomes to expect (Wyatt 2008; Krivov 2010; Kenyon and Bromley 2016; Lee and Chiang 2016; Bonnefoy et al. 2021).

Debris discs are usually modelled with a source population as a belt of planetesimals undergoing

collisional evolution, where the velocity dispersion is stirred either by the development of larger bodies within the belt, or as the result of perturbations from planets in the system (e.g., Wyatt 2008). These are natural analogues of the Solar system dust generated either by collisions in the Asteroid belt or the Kuiper belt, although the extrasolar systems are much more massive.

However, there is a third Solar System small body population that is thought to have undergone substantial collisional evolution but has not yet been widely considered in the extrasolar context – namely the irregular satellites of the giant planets (Jewitt and Haghighipour 2007). Evolutionary models of this population suggest that it could have been much larger in the past and could have generated ~0.001 lunar masses of dust per giant planet (Bottke et al. 2010). Indeed, such populations are thought to be an inevitable consequence of giant planet formation (Nesvorný et al. 2007) and the possible existence of irregular satellite clouds around extra-solar planets has recently been postulated to explain the curious properties of the exoplanet candidate Fomalhaut b (Kennedy and Wyatt 2011; Kenyon and Bromley 2016). These papers have focussed on the production of dust near the planet, but radiation pressure forces will cause much of the dust to spiral outwards into a circumstellar ring, and can therefore also contribute to the observed extended structures observed around many stars.

Therefore, our goal in this paper is to examine the kinds of debris disc signatures one might expect from a source population initially confined to a planetary Hill sphere, and to explore their similarities and differences with those that result from more traditional population assumptions. An alternative to the traditional planetesimal disc model is particularly attractive in the case of the radially thinnest debris rings, such as those around Fomalhaut and HR 4796A, where the narrowness requires additional hypotheses such as shepherd satellites (Boley et al. 2012), instabilities involving a gaseous component (Lyra and Kuchner 2013) or recent collisions (Olofsson et al. 2019). We will demonstrate that irregular satellite clouds naturally give rise to narrow rings and may therefore offer a more natural explanation for these structures, in the sense that the confinement of the original planetesimal population is due to the gravitational influence of the planet.

The outline of this paper is as follows. In § 2 we describe the dynamics of radiation pressure-

driven dust in the reduced three-body problem, and examine the debris disc geometry that results if the source population of the dust is initially restricted to a planetary Hill sphere. In § 3 we then introduce a model for a source population of dust which we combine with the dynamical model to build a model of a candidate debris disc so that we may explore the observational implications of this hypothesis. We then compare these features to the present state of the art observations of the two most prominent thin ring systems – Fomalhaut and HR 4796A – in § 5.

CHAPTER 2

Dynamics of Dust Generated in an Irregular Satellite Swarm

The scattering, absorption, and re-emission of light in a debris disc is the action of dust particles in orbit about the star. In a traditional debris disc model, this dust is released in collisions between larger bodies in heliocentric orbits, and so reflects the heliocentric distribution of the parent bodies. Here we wish to examine the consequences when the dust is released by collisions between bodies that are localised in orbit around a planet. In addition to the radiation pressure force from the central star, their dynamics is also regulated by the gravitational influence of the planet.

2.1 Single Dust Grain Dynamics in the Restricted Three-Body Problem with Radiation Pressure

Dust particles have infinitesimal mass, so their dynamics can be treated accurately within the paradigm of the restricted three-body problem, sketched out in Fig. 2.1 (Murray and Dermott 1999). However, the stream of photons emanating from the central star is absorbed or scattered by the dust grains, and exerts a radiation pressure. This means that small particles experience a non-negligible additional radial force, which reduces the effective gravity of the central object (Schuerman 1980) and fundamentally alters the geometry of the pseudo-potential that regulates the dynamics. We can relate this purely radial radiation pressure force to the stellar gravitational force using the formalism of Burns et al. (1979) as follows,

$$\boldsymbol{F} = -\frac{G(1-\beta)M_1 m}{r_{13}^2}\hat{\boldsymbol{r}}_{13} - \frac{GM_2 m}{r_{23}^2}\hat{\boldsymbol{r}}_{23}, \tag{2.1}$$

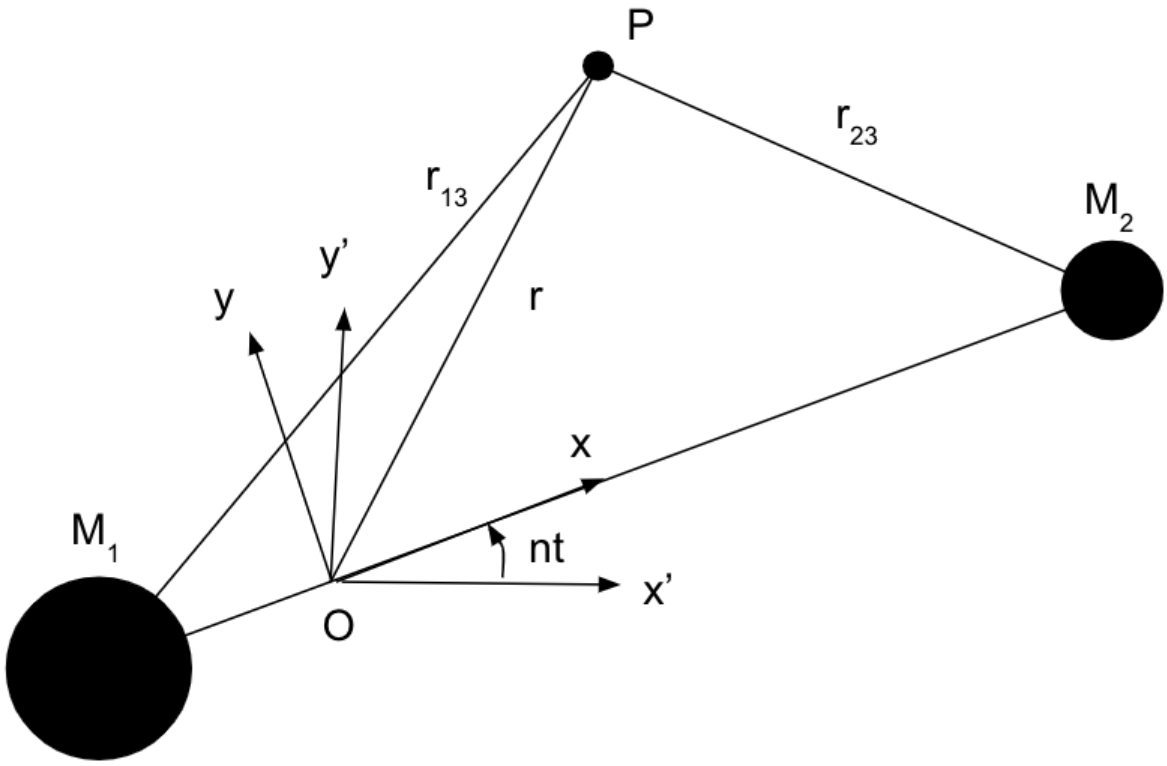

Figure 2.1: Schematic of the restricted three-body problem. The x- and y-axes make up the co-rotating centre-of-mass frame, rotating at an angular velocity n, centered at point O. The x'- and y'-axes make up the inertial centre-of-mass frame. M_1 and M_2 are massive bodies with the third body located at point P.

where G is the Newtonian gravitational constant, $\beta = |\boldsymbol{F}_{\rm rad}|/|\boldsymbol{F}_{\rm grav}|$ is the relative strength of radiation pressure compared to stellar gravity, M_* is the stellar mass, m is the dust grain mass, r_{13} is the distance from the grain to the star, r_{23} is the distance from the grain to the planet, $\hat{\boldsymbol{r}}_{13}$ is the radial unit vector away from the star toward the grain, and $\hat{\boldsymbol{r}}_{23}$ is the radial unit vector away from the planet toward the grain. For $\beta > 0$, the dust grains behave as if they 'see' a star of reduced mass $(1-\beta)M_*$.

The parameter β reflects the strength of the radiation pressure, and can be more precisely quantified as

$$\beta = \frac{3L_*\langle Q_{\rm rad}\rangle}{8\pi G M_* c \rho D}, \tag{2.2}$$

where L_* is the stellar luminosity, $\langle Q_{\rm rad}\rangle$ is the wavelength-averaged radiation pressure coefficient, c is the speed of light, ρ is the mass density of grains, and D is the diameter of the grain. This β can be thought of as a proxy for grain size D if we assume a constant mass density ρ among dust grains, since $\langle Q_{\rm rad}\rangle$ is of order unity. Koschny and Grün (2001) performed laboratory experiments involving collisions between silicates and found the mass density of resulting grains to be $\rho = 2.8$ g cm^{-3}. We assume a value for $\langle Q_{\rm rad}\rangle \sim 0.5$ as a rough average from Liu and Schmidt (2018). β can thus be evaluated as

$$\beta \approx 0.17\left(\frac{D}{10\ \mu{\rm m}}\right)^{-1}\left(\frac{L_*}{16\ {\rm L}_\odot}\right)\left(\frac{M_*}{1.92\ {\rm M}_\odot}\right)^{-1}, \tag{2.3}$$

where we have assumed typical values of luminosity and mass of an A-type star such as Fomalhaut.

The dynamics of the test particle in the co-rotating frame of the reduced three-body problem is governed by a pseudo-potential that accounts for both the gravity of the two massive bodies and the centrifugal force (Murray and Dermott 1999). The pseudo-potential defines a set of 'zero-velocity curves' which restrict the motion of a test particle, depending on its initial conditions.

The fact that the radiation pressure only scales the effective mass of the central star means that the same formalism applies here, but the revision of the coefficients in the pseudo-potential results

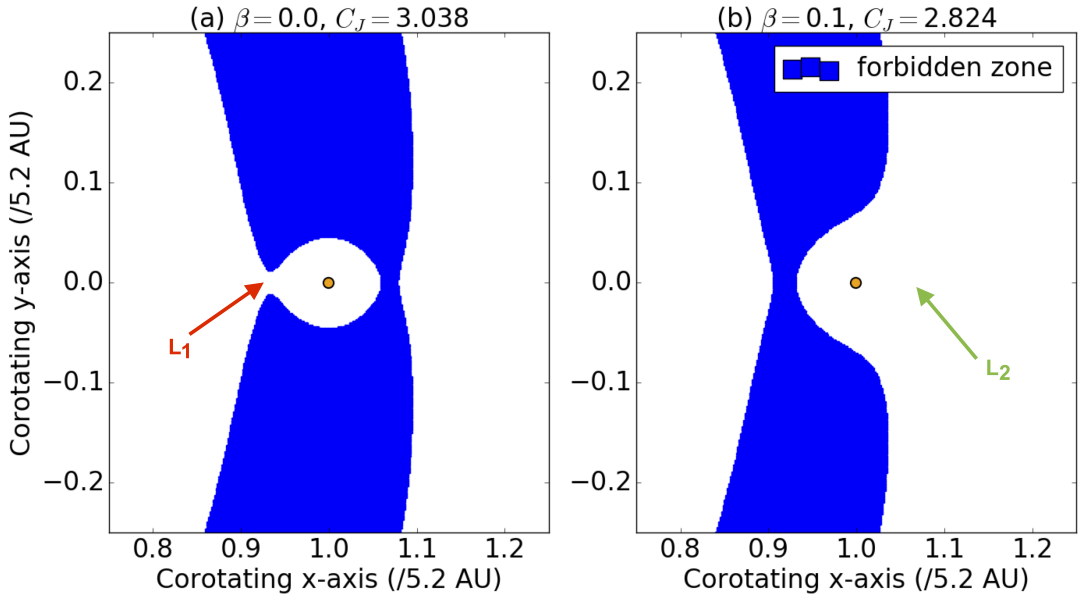

Figure 2.2: *Panel (a):* forbidden zone (in blue) for a Jacobi constant of $C_J = 3.038$ when radiation pressure is not included ($\beta = 0$). *Panel (b):* forbidden zone (in blue) for a Jacobi constant of $C_J = 3.824$ when radiation pressure is taken into account ($\beta = 0.1$). The orange circle (not to scale) represents the location of the giant planet. In panel (a), we note that the Hill spheres of the star and planet overlap at the L_1 Lagrange point. Thus, dust grains originating in the planetary Hill sphere are permitted to escape into a circumstellar orbit. In contrast to panel (a), we note that in panel (b), there is now an opening at the L_2 Lagrange point for the dust grains to escape from.

in an important qualitative difference. Although the direct gravitational force felt by the dust is reduced by the radiation pressure, the orbital velocity of the planet is not similarly affected, and so the relative contributions of the three different components of the pseudo-potential change with β. In particular, at fixed mass, there is a critical β above which the L_2 point becomes the global potential minimum (instead of L_1, as in the $\beta = 0$ case). This distinction is important because it is this minimum that decides the direction in which dust, grinding down in a collisional cascade, leaves the Hill sphere and enters heliocentric orbit.

To illustrate the effects of this change in geometry, let us consider two different physical scenarios: one where radiation pressure is not important (i.e., turned 'off,' $\beta = 0$) as in panel (a) of Fig. 2.2 and another where radiation pressure is important (i.e., turned 'on') as in panel (b) of Fig. 2.2. Without loss of generality, we take $\beta = 0.1$ for the radiation pressure scenario. If we wish to derive the minimum velocity of escape, we see that, in panel (a), particles will more readily escape through the L_1 Lagrange point than L_2. This behavior is well studied, such as in the case of Roche lobe overflow where mass transfer can occur between two bodies in a binary system. However, when radiation pressure is non-negligible, we see in panel (b) that the lowest velocity particles to escape now overflow L_2. Thus, the addition of radiation pressure into our equations of motion changes the physics from accretion on to the star to ejection of material outside the orbit of the planet. This is a consequence of the weakened effective gravity of the central star, which shifts its contribution to the pseudo-potential inwards and changes the relative heights of the L_1 and L_2 points. In Appendix A we review more thoroughly how this change in topology occurs as β is changed.

There are essentially three fates for a dust grain: (i) accretion on to the planet, (ii) accretion on to the star, or (iii) escaping to infinity. Depending on the initial conditions, the dust grain may simply spiral into the planet after an irregular satellite collision, coating the planet, and any satellites, with dark dust and affecting its albedo (Burns et al. 1979; Bottke et al. 2010). Accretion on to the star may occur as the result of another radiation-related process: Poynting-Robertson (PR) drag. This is a consequence of the loss of angular momentum due to reradiation of absorbed energy by the

dust, but is not taken into account here because it occurs on a longer time-scale than the direct dynamical effects of radiation pressure, and generally affects large particles more.

For our purposes, the most important outcome is escape from the Hill sphere through the L_2 point. Although the eventual outcome is escape to infinity, orbital integrations show that many trajectories spend multiple orbital periods in the vicinity of the outer edge of the relevant zero-velocity curve, before eventually spiralling outwards. This extended period of quasi-regular orbital behaviour thus gives rise to the observational appearance of a thin ring, allied with an exponential tail of orbits that extend out much farther. Such a configuration bears a qualitative resemblance to the 'birth ring + halo' model of many debris systems and we will examine its observational consequences below.

2.2 Sample Orbital Integrations

To better understand how this change in geometry reflects itself in orbital behaviour, let us examine the behaviour of a few representative test particles before building a large ensemble population. We perform our numerical integrations using the MERCURY N-body integrator (Chambers 2012). We start with the simplest case of $\beta = 0$, which represents a particle that is too large for radiation pressure to have an appreciable effect. Each particle originates in the Hill sphere of its parent planet, and receives a 3-D velocity vector of magnitude v_i, whose direction is oriented randomly. (We also investigated the effects of preferring prograde or retrograde orbits for our initial conditions, but found no significant change in the results compared to randomly oriented orbits.) After a few orbits around the planet many grains slip through the L_1 Lagrange point and 'bounce' along the inner edge zero-velocity curve. After several excursions around the star, the grain returns to the Hill sphere through the L_1 orbit in a messy, rapidly precessing orbit. In the absence of a dissipative mechanism, this behavior basically repeats itself over time, with the grain being gravitationally shared by the star and the planet. On longer time-scales, Poynting-Robertson drag will eventually decouple the particle from the Hill sphere and it will spiral into the star.

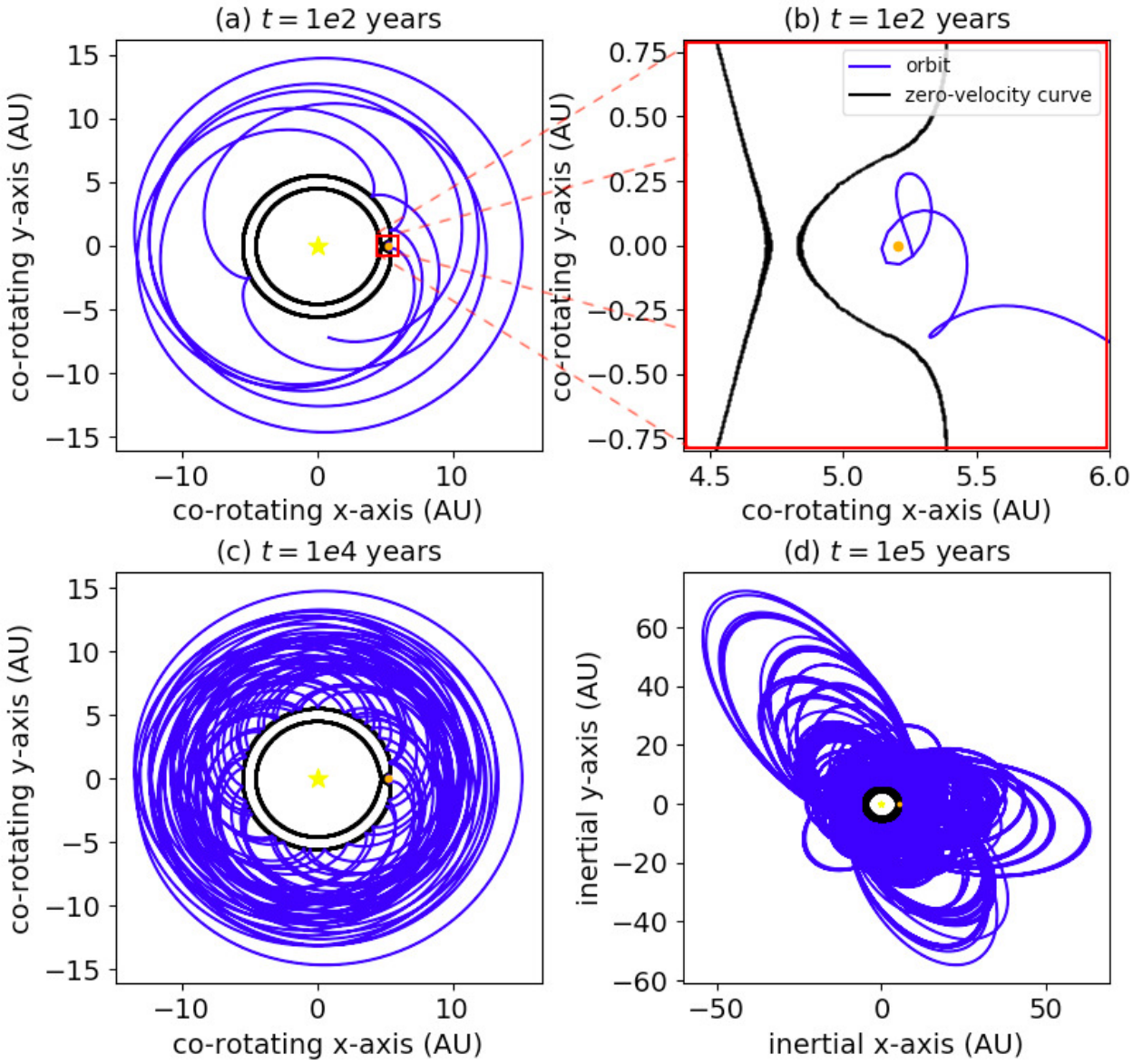

Figure 2.3: Orbital trajectory of a single 1 μm dust grain (in blue) overplotted on its respective $\beta = 0.1$ zero-velocity curves (in black). The orbits are shown at various evolutionary stages: $t = 1e2$ yr in panels (a)–(b), $t = 1e4$ yr in panel (c), and $t = 1e5$ yr in panel (d). Panel (b) represents a zoom-in of panel (a).

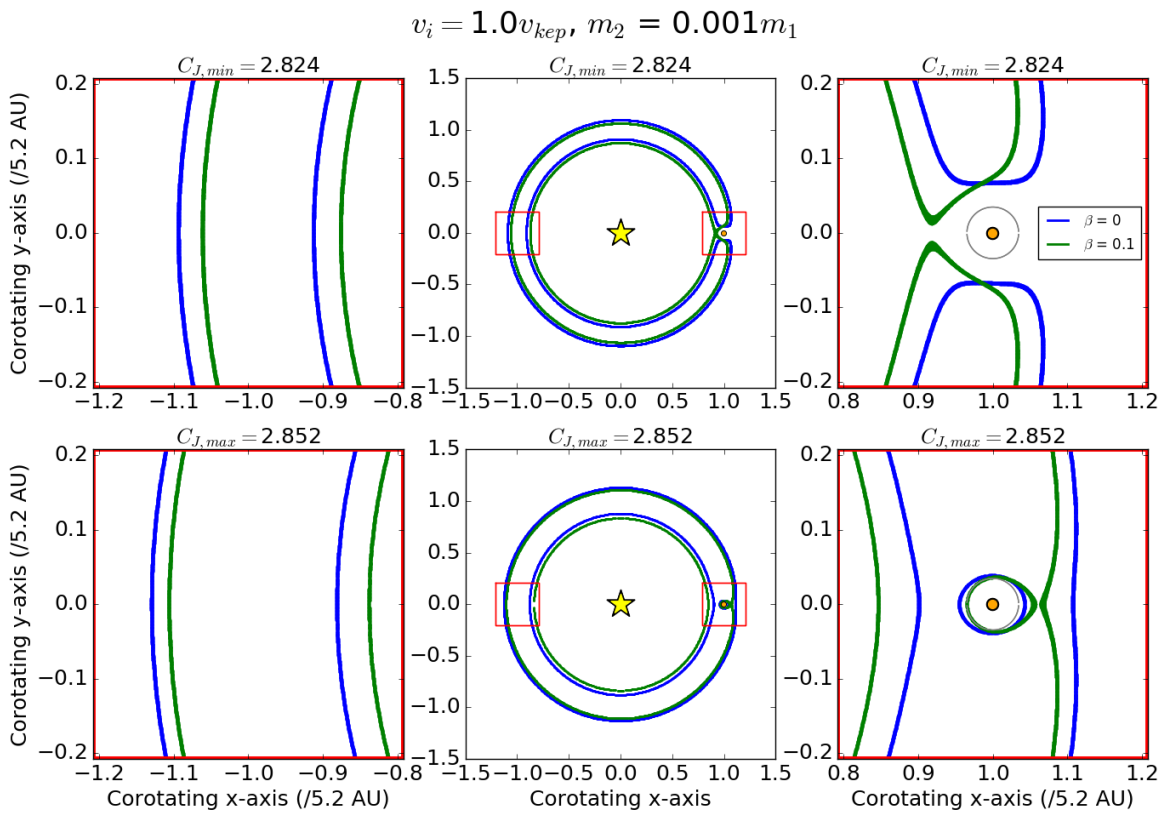

Figure 2.4: Zero-velocity curves for both the classic restricted three-body problem ($\beta = 0$) and with moderate radiation pressure included ($\beta = 0.1$), as representative examples for a mixed mass ratio of $M_2/M_1 = 0.001$. The left and right columns represent zoomed in versions of the respective red squares shown in the middle column. The top row shows the contours for the minimum Jacobi constant that arises from the initial conditions while the bottom row shows that contours for the maximum Jacobi constant. Thus, all possible Jacobi constants fall between these two extrema. The main two findings here are that the forbidden zone thickness increases with increasing radiation pressure, but the radii of both the inner and outer edges of the forbidden zone shrink with increasing radiation pressure, as seen in the left column. In other words, the radius of the outer edge of the forbidden zone shrinks less than that of the inner edge.

Next we examine the case of radiation pressure turned 'on' with an intermediate strength of $\beta = 0.1$. The path of such a particle is shown in Fig. 2.3, for the case of a Jupiter mass planet on a circular orbit of semi-major axis 5 au. In this case, the particle spirals outwards – rather than inwards – and makes several cardiod-shaped excursions, roughly several planetary semimajor axes in size, as shown in panel (a). This is a consequence of the aforementioned change in the geometry of the pseudopotential, as shown in panel (b). Like in the $\beta = 0$ case, the grain will occasionally come to a sharp halt along the predicted zero-velocity curve. However, the fundamental alteration of the forbidden zone, caused by the addition of radiation pressure, means that the 'collision' occurs with the outer edge of the zero-velocity curve, not the inner one. In panel (c), we see that after a moderate number of dynamical time-scales, this behavior essentially repeats itself since the orbits all stay within ~15 au. However, in panel (d), after a large number of dynamical time-scales, we see that the eccentricity of the grain has been pumped up dramatically, reaching an apoapsis up to ~75 au, until it is effectively ejected from the system.

These sample integrations illustrate that the dynamics of particles released from the planetary Hill sphere under the influence of radiation pressure can reproduce the basic birth ring configuration of debris disc models, even without the underlying birth ring of planetesimals. We wish now to expand this into a proper model for debris discs. This means we need a more detailed source model, which will link the properties of the dust to the new underlying planetesimal population – the irregular satellite population. This is the focus of § 3.

2.3 Forbidden Zone Thickness as a Function of Radiation Pressure

An interesting question is to ask how the results of our simulations will change depending on planet mass, since the study of exoplanets around nearby stars has discovered a great variety in planetary properties. The solutions to the restricted three-body problem depend not just on the mass of the secondary body (the planet), but specifically on the mass ratio of the secondary body to the primary body ($\mu = M_1/M_2$). Thus, a Saturn-like planet orbiting an M dwarf may have similar dynamics to

those of a Jupiter-like planet orbiting a Sun-like star, if both systems have a mass ratio of $\mu \sim 0.001$.

Increasing radiation pressure generally has the effect of increasing the forbidden zone thickness as seen in the first column of Fig. 2.4. However, while the overall thickness increases, we can see that the radii of both the inner and outer edge of the forbidden actually decrease. In other words, the radius of the outer edge is decreasing by a smaller amount than that of the inner edge.

For a more comprehensive look at how the forbidden zone changes as a function of both radiation pressure strength and mass ratio, interested parties may refer to the discussion in Appendix B.

CHAPTER 3

Generation of Dust in an Irregular Satellite Swarm

We assume that the particles whose orbits we track originate from collisions between irregular satellites orbiting around the giant planet. Irregular satellites revolve around their parent planet at relatively large distances compared to other moons (e.g., Bottke et al. 2010), so it is natural to characterize their distances in units of Hill radii, given by $R_{\rm H} = a_{\rm p}[M_{\rm p}/(3M_*)]^{1/3}$, where $a_{\rm p}$ is the planetary semimajor axis and $M_{\rm p}$ is the planetary mass. The original orbits of irregular satellites are believed to be roughly isotropically distributed (Jewitt and Haghighipour 2007), so we investigate both prograde and retrograde orbits around the parent planet, which are typically found at $r_{23}/R_{\rm H}$ values of $\sim$ 0.1 to 0.5, where r_{23} is the distance between the planet and the dust grain. Thus, we use those upper and lower limits to randomly generate starting locations for the dust grains.

We divide the discussion of initial velocities into magnitude and direction. We take the magnitude of the velocity to be the Keplerian circular velocity at the debris's respective distance from the planet. Since it is a spherically symmetric cloud, we assume that the direction of the dust grain's velocity unit vector is random. Specifically, in polar coordinates θ and ϕ, $\cos(\theta)$ is distributed uniformly in [-1,1) and ϕ is distributed uniformly in [0,2π). We find no significant difference between the qualitative results for orbits that are initially prograde or retrograde. Since the Keplerian velocity is given by $v_{\rm kep} = (GM_{\rm p}/r_{23})^{1/2}$, the initial velocities are given by

$$v_{\rm kep} = (2.248 \text{ km s}^{-1})\left(\frac{M_{\rm p}}{\rm M_J}\right)^{1/2}\left(\frac{r_{23}}{0.5\ R_{\rm H}}\right)^{-1/2} \tag{3.1}$$

where $\rm M_J$ is the mass of Jupiter.

3.1 Rate of Dust Generation

A population of irregular satellites will generate a collisional cascade, in which planetesimals are ground down to micron-sized dust grains. Collisions between the largest collisionally coupled bodies of size $D_{\max}$ initiate the cascade, creating numerous medium-sized bodies that further collide with each other to produce successively smaller bodies. In the traditional context of a circumstellar debris disc, the smallest collisionally coupled body's size $D_{\min}$ is determined by the strength of the central star's radiation pressure, and tends to be about 1 micron. This is often referred to as the blowout size. Dohnanyi (1969) found that a self-similar, steady-state cascade follows a power law differential size distribution governed by

$$\frac{dN}{dD} \propto D^{-q}, \tag{3.2}$$

where D is the spherically symmetric grain's diameter and $q \approx 3.5$. A dust grain is no longer in a bound orbit around the star when the ratio of radiation pressure force to gravitational force is greater than 0.5 (e.g., Pawellek and Krivov 2015), i.e.,

$$\beta \equiv \frac{F_{\text{rad}}}{F_{\text{grav}}} \geq 0.5. \tag{3.3}$$

In the case discussed here, there is an additional consideration. Fragments from irregular satellite collisions will continue to participate in the collisional cascade as long as they orbit within the planetary Hill sphere. However, once the radiation pressure is strong enough for the particle to escape the Hill sphere, the density of collision targets drops dramatically and the collisional time-scale becomes large. Thus, the minimum particle size in the cascade is set by the size for which the residence time within the Hill sphere equals the characteristic collision time for particles of that size. The residence time here is defined as the amount of time a dust grain spends in the Hill sphere at a given β before escaping. Conversely, this also sets a minimum β for the particles in the more extended debris disc and thus regulates their size.

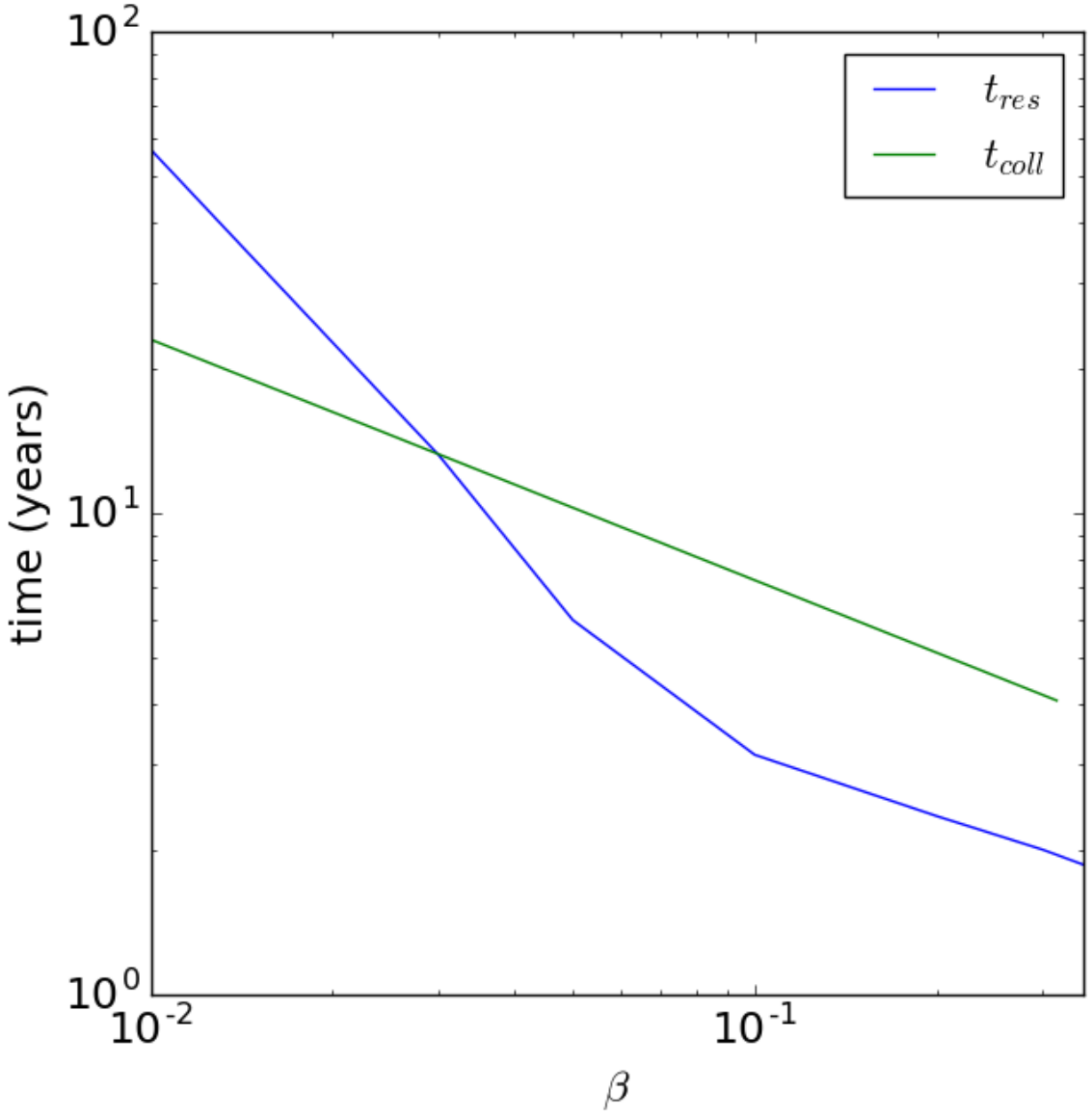

Figure 3.1: Characteristic dust grain residence time in the Hill sphere (in blue) – derived from numerical integration of orbits – and catastrophic collisional time-scale (in green) – from equation (3.4), both as functions of β. The intersections of the curves at approximately $\beta = 0.03$ represents the critical size at which a dust grain can decouple from the collisional cascade and be expelled from the Hill sphere.

We can find the collisional time-scale $t_{\rm coll}$ for any member of the collisional cascade from $t_{\rm coll} = 1/(n\sigma v_{\rm rel})$, where n is the number density of particles, σ is the cross section, and $v_{\rm rel}$ is the relative velocity between impactors. The number density of particles is given by $n = N/V$, where N is the number of particles and V is the volume they occupy. Since the irregular satellites are distributed isotropically in a spherical cloud, we take this volume to be some spherical shell with the radius the fraction $f_{\rm tot}$ of the Hill radius they occupy: $V = f_{\rm tot} V_H = f_{\rm tot}(4\pi/3)R_{\rm H}^3$. Gravitational focusing is not important for submillimeter-sized particles, the cross section is just the geometric cross section: $\sigma = \pi(D/2)^2$. Lastly, we take the relative velocity $v_{\rm rel}$ to be of order the keplerian velocity $v_{\rm kep}$ since the orbital inclinations of irregular satellites are randomly oriented. Putting everything together, we find that the collisional time-scale is

$$\begin{aligned} t_{\rm coll} = (726\ {\rm yr})&\left(\frac{\beta}{0.1}\right)^{-1/2}\left(\frac{M_{\rm tot}}{10^{-2}{\rm M_L}}\right)^{-1}\left(\frac{\rho}{1\ {\rm g\ cm^{-3}}}\right)^{1/2} \\ &\times\left(\frac{D_{\rm max}}{100\ {\rm km}}\right)^{1/2}\left(\frac{M_*}{\rm M_\odot}\right)^{-5/3}\left(\frac{M_{\rm p}}{\rm M_J}\right)^{-2/3}\left(\frac{L_*}{\rm L_\odot}\right)^{1/2} \\ &\times\left(\frac{\langle Q_{\rm rad}\rangle}{0.5}\right)^{1/2}\left(\frac{a}{\rm a_J}\right)^{7/2}\left(\frac{f}{0.4}\right)^{1/2}\left(\frac{f_{\rm tot}}{0.098}\right), \end{aligned} \tag{3.4}$$

where $M_{\rm tot}$ is the total mass of the collisional cascade, $\rm M_L$ is lunar masses, $\rm a_J$ is the semimajor axis of Jupiter, f is the orbital radius of the body as a fraction of the Hill radius ($f = r_{23}/R_{\rm H}$). As long as the residence time $t_{\rm res}$ is larger than the collisional time-scale $t_{\rm coll}$, we expect the grains to continue to grind down to smaller sizes, which increases β and shortens the residence time-scale. We calculate $t_{\rm res}$ by averaging over a large number of trajectories, as a function of β.

Fig. 3.1 shows the comparison of characteristic collisional and residence time-scales for the dust generated in irregular satellite collisions for a Jupiter-like planet orbiting a Sun-like star. At low β (large particles), the residence time within the Hill sphere is long, because radiation pressure is weak, but as β increases, the residence time falls sharply as the radiation pressure accelerates the exodus. Although the collision time also gets shorter with decreasing size, the dependence is flatter. The net result is that the cascade to smaller size is truncated when β is large enough that the particles exit the Hill sphere before undergoing any more collisions.

3.2 Source Model

Our integrations yield a large number of trajectories as a function of time, for different β. A realistic model assumes that individual dust grains are generated at a constant rate due to the collisional cascade initiated by the irregular satellite population. In practice, we achieve this continuous generation by offsetting the initial time of individual grain trajectories from our library of integrations. Working within the co-rotating frame ensures that new dust grains will always be produced in the Hill sphere of the planet. We then track the dynamical evolution of these dust grains to calculate density profiles of the dust population, as described in the next section.

CHAPTER 4

Results

The irregular satellite source model for generating dust discs is fundamentally different from the traditional planetesimal disc source population in that it has a localised source region, confined within the planetary Hill sphere, from which the material spreads out slowly. In this chapter we wish to therefore characterise the observational appearance of the resulting dust population, which we term an ISDD (Irregular Satellite Debris Disc).

4.1 From Circumplanetary to Circumstellar Orbits

Fig. 4.1 shows a snapshot of the positions of $N = 750,000$ particles with $\beta = 0.1$, integrated for 10^3 planetary dynamical times (~12,000 yr). The distribution of dust grains can be divided into circumstellar material and circumplanetary material. The circumstellar material is made up of dust grains that were able to escape from the Hill sphere whereas circumplanetary material represents grains that are still trapped in the Hill sphere. Whether or not a dust grain successfully escapes from the Hill sphere is primarily determined by initial conditions. The role of the zero-velocity curves from the Jacobi formalism in shaping the distribution of the escaped material is clear. Aspects of this dust population, such as azimuthal symmetry, radial profile, ring thickness, and vertical profile will be examined in the following sections.

It is important to note that the overdensity within the Hill sphere in Fig. 4.1 is artificial because those particles, that do not escape, will be subjected to continued collisional evolution not included in this simulation, and the particles are shown here primarily to illustrate the nature of the dust

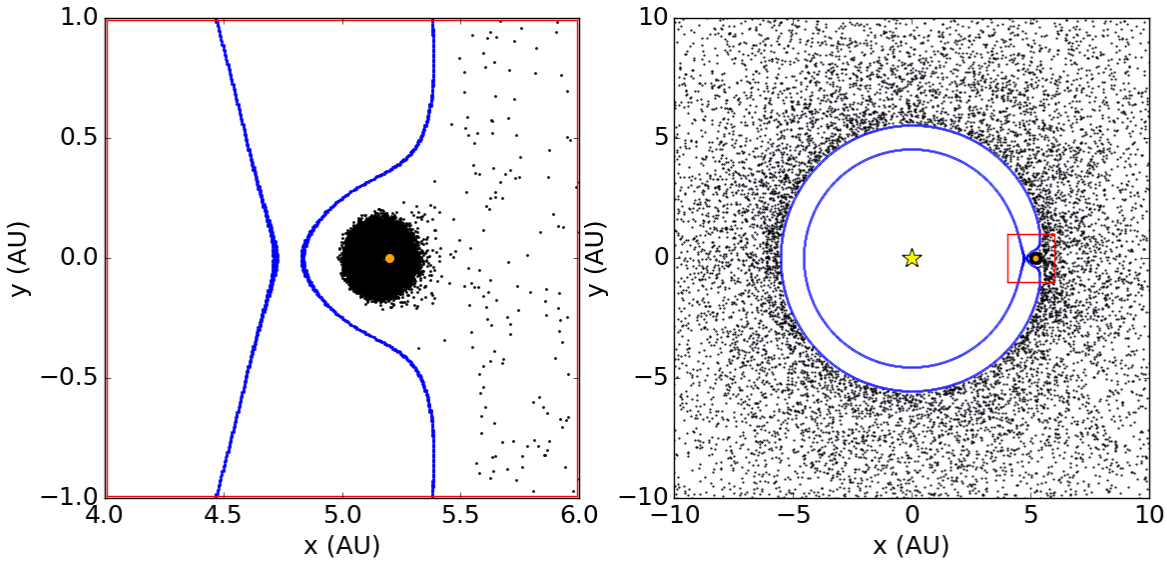

Figure 4.1: Position of test particles moving under the influence of radiation pressure for a value of $\beta = 0.1$ after 1,000 dynamical time-scales of integration. The zero-velocity curves for $C_J = 2.824$ are plotted in blue. The location of the star and planet are denoted by a yellow star and orange dot respectively. The right panel shows an edge-on view of the disc as a whole. The left panel zooms in on the vicinity of the planet, showing an overdensity of material in the Hill sphere. These are particles whose trajectories remain bound over the course of the simulation. In reality, these particles have orbited the planet for hundreds of collisional times and will have been ground down to much smaller sizes. Therefore, it is important to note that the overdensity within the Hill sphere is not physical, and is shown here primarily to illustrate the nature of the dust trajectories and their evolution. When viewed as a synthetic image, the panel on the right should have the circumplanetary excess reduced by a factor of several hundred, at least.

trajectories and their evolution. As we previously saw in Fig. 3.1, the intersection of the residence time and collisional time-scale occurs at a very short time-scale (<100 yr). This is very short compared to the duration of the simulation (~12,000 yr), so we expect trapped dust grains to still be coupled to the original cascade, grinding down to even smaller sizes until they too are blown out of the Hill sphere. As a result, we would not expect to see a pileup of material in the form of a circumplanetary disc.

4.2 ISDDs are Azimuthally Symmetric

Although the dust is initially generated within the Hill sphere, once it escapes, azimuthal symmetry in an ISDD is achieved very quickly. Fig. 4.2 shows the azimuthal profile of the dust after 100 dynamical time-scales, in the case of $\beta = 0.1$. We have intentionally excluded material that remains the planetary Hill sphere so that the global circumstellar disc features could be examined.

We quantify the baseline fluctuations in the azimuthal profile by comparing the mean value to the standard deviation. We conclude for eight representative values of β in the range $0.01 \leq \beta \leq 0.35$ that the ISDDs are azimuthally symmetric since the standard deviations are small compared to the mean. For example, in the case of $\beta = 0.01$, the average number of dust grains per bin is 229.2 while the standard deviation is 17.2, so we conclude that the variations are small. Similar results are obtained for other values of β. Dust rings generated in this manner nevertheless retain the appearance of azimuthal symmetry.

Another way to evaluate the azimuthal symmetry of the disc is to calculate the average dust grain semimajor axis as a function of azimuthal angle θ. In Fig. 4.2, we calculate both the mean and the median radius for the $\beta = 0.05$ disc. We find that the mean radius (in blue) is approximately 12 au and that the median radius (in green) is approximately 8 au. It is not surprising to see that the mean radius is higher than the median radius. While the vast majority of dust grains spend their time close to the planet's orbit bouncing around the edges of the Jacobi contours, a small fraction of dust grains will be spiraling out of the system due to the influence of radiation pressure, biasing

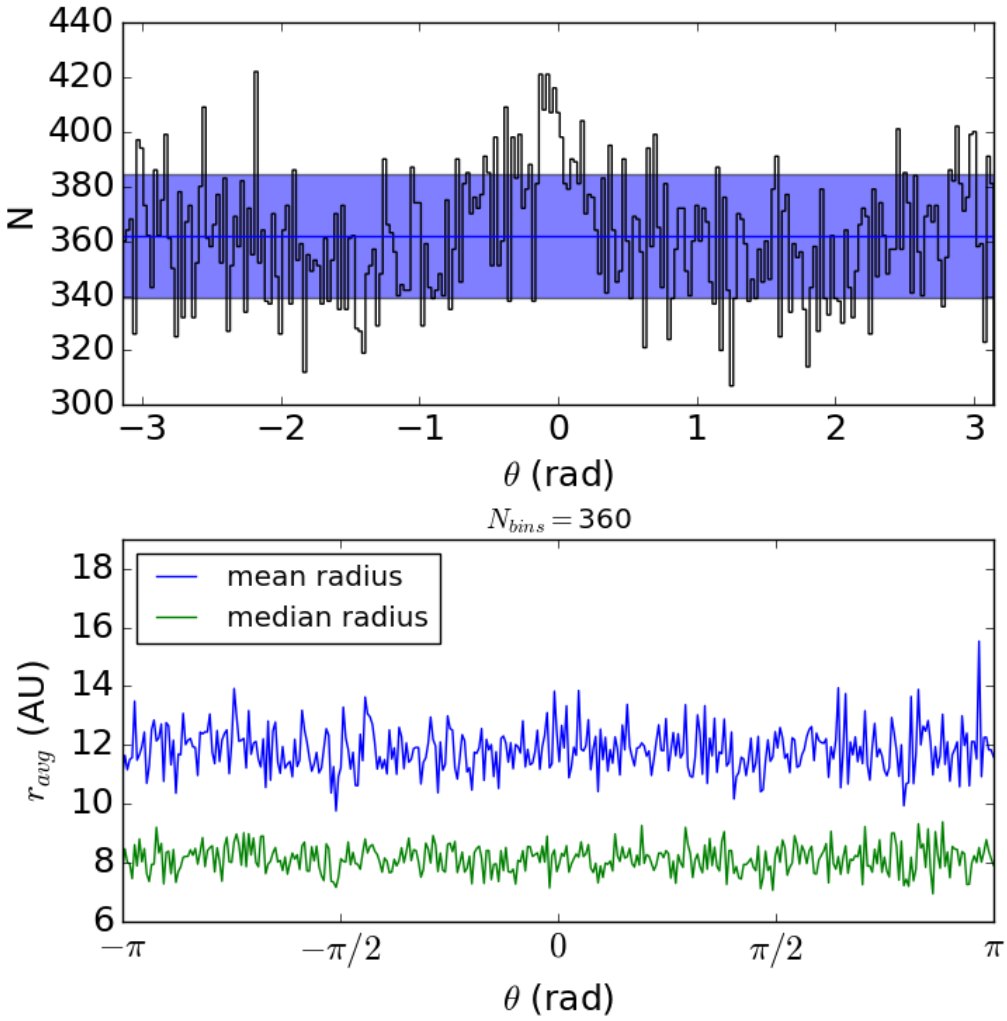

Figure 4.2: *Top:* Histogram of dust grain distribution as a function of azimuthal angle θ for $\beta = 0.05$. The spike located at $\theta = 0°$ has been subtracted off, since leftover material in the planetary Hill sphere is not part of the circumstellar disc. The average number of dust grains per bin is 362 with a standard deviation of only 23 grains, denoted by the horizontal blue line and blue shaded region. *Bottom:* Mean and median radius as a function of azimuthal angle θ. The mean radius is approximately 12 au at nearly all angles while the median radius is approximately 8 au at all angles, showing that the disc is very azimuthally symmetric.

the mean to higher radii.

4.3 ISDDs Exhibit Thin Ring Morphology

Astronomers commonly quantify ring thickness as the ratio of ring width to ring radius $\Delta R/R$. Specifically, a ring is characterized as 'thin' if $\Delta R/R < 0.2$. This definition takes into consideration the great diversity of size scales that debris discs are observed to span and allows us to compare systems on large and small absolute scales. However, the ratio requires us to specify how we define ΔR and R. We first fit a function to the distribution and find that several of the parameters naturally characterize the ring width and ring radius.

Specifically, we fit a piecewise function to the radial profile that contains three physically motivated regimes. Region I ($r_{13} < r_{\rm A}$) is simply a one-sided gaussian that describes the sharp inner edge of the ring. This feature is to be expected since the forbidden zones from the Jacobi contours prevent dust grains from wandering any closer to the star than one planetary semimajor axis plus one Hill radius ($a + R_{\rm H}$). Region II ($r_{\rm A} < r_{13} < r_{\rm B}$) is an exponential decay function that describes the initial drop off in surface density that occurs as we move outward away from the peak. The peak tends to be just outside of the Jacobi contours because the dust grains spend a lot of time bouncing around the edges of the zero-velocity curves before they are ejected from the system. Lastly, Region III ($r_{13} > r_{\rm B}$) is a continuation of Region II with an added exponential term to soften the dropoff and match the more gradual decay of the outer edge. This feature is also expected since we are investigating moderate radiation pressure strengths ($\beta = 0.05 - 0.35$) that are strong enough to perturb the dust grains from a circumplanetary orbit to a circumstellar orbit, but not strong enough to immediately eject the grains from the system. The gradual tail of the radial distribution represents dust grains that are in the process of slowly spiraling out of the system. A sample fitted radial profile for $\beta = 0.15$ is shown in Fig. 4.3. The resulting functional form is

$$N(r_{13}) = \begin{cases} N_0 \exp\left(-\dfrac{(r_{13}-r_{\rm A})^2}{2\sigma_1^2}\right), & r_{13} \le r_{\rm A} \\ N_0 \exp\left(-\dfrac{(r_{13}-r_{\rm A})}{\sigma_2}\right), & r_{\rm A} < r_{13} < r_{\rm B} \\ N_0 \exp\left(-\dfrac{(r_{13}-r_{\rm A})}{\sigma_2}\right) & \\ \quad + N_1\left[1 - \exp\left(-\dfrac{(r_{13}-r_{\rm B})}{\sigma_3}\right)\right], & r_{13} > r_{\rm B} \end{cases} \tag{4.1}$$

where N_0 and N_1 are normalization constants for their respective terms, $r_{\rm A}$ is the peak of the distribution, $r_{\rm B}$ is the transition point between Regime II and Regime III, σ_1 is the standard deviation of the single-sided gaussian, and σ_2 and σ_3 are the characteristic lengths of their respective exponential decay terms.

In order to cast this in the observational variables ΔR and R, we take $R \equiv r_{\rm A}$ since it naturally describes the peak of the distribution, and $\Delta R \equiv \sigma_1 + \sigma_2$ since those lengths each characterize the dropoff in either direction away from the peak. Thus, in terms of the function parameters, $\Delta R/R \equiv (\sigma_1 + \sigma_2)/r_{\rm A}$.

We also apply the fit to multiple homogeneous discs of different values of β ($\beta = 0.05 - 0.35$). We measure their normalized ring widths and determined the uncertainty by marginalizing out the seven parameters in the function described above in favor of $\Delta R/R$. A 3σ confidence interval was used to determine the upper and lower limits of the ensuing error bars. Those results are summarized in Fig. 4.4. The general trend is that the thickness of the ring grows with increasing β. This occurs because higher values of β correspond to stronger radiation pressure. This stronger pressure is able to more efficiently push dust grains into larger and more eccentric orbits.

4.4 An Exponential Tail

As mentioned in the previous section, the radial distribution has a gently sloped exponential tail. This tail is a generic feature of all models that take radiation pressure into account. However, our model generate larger particles than a standard source model since the collisional cascade is

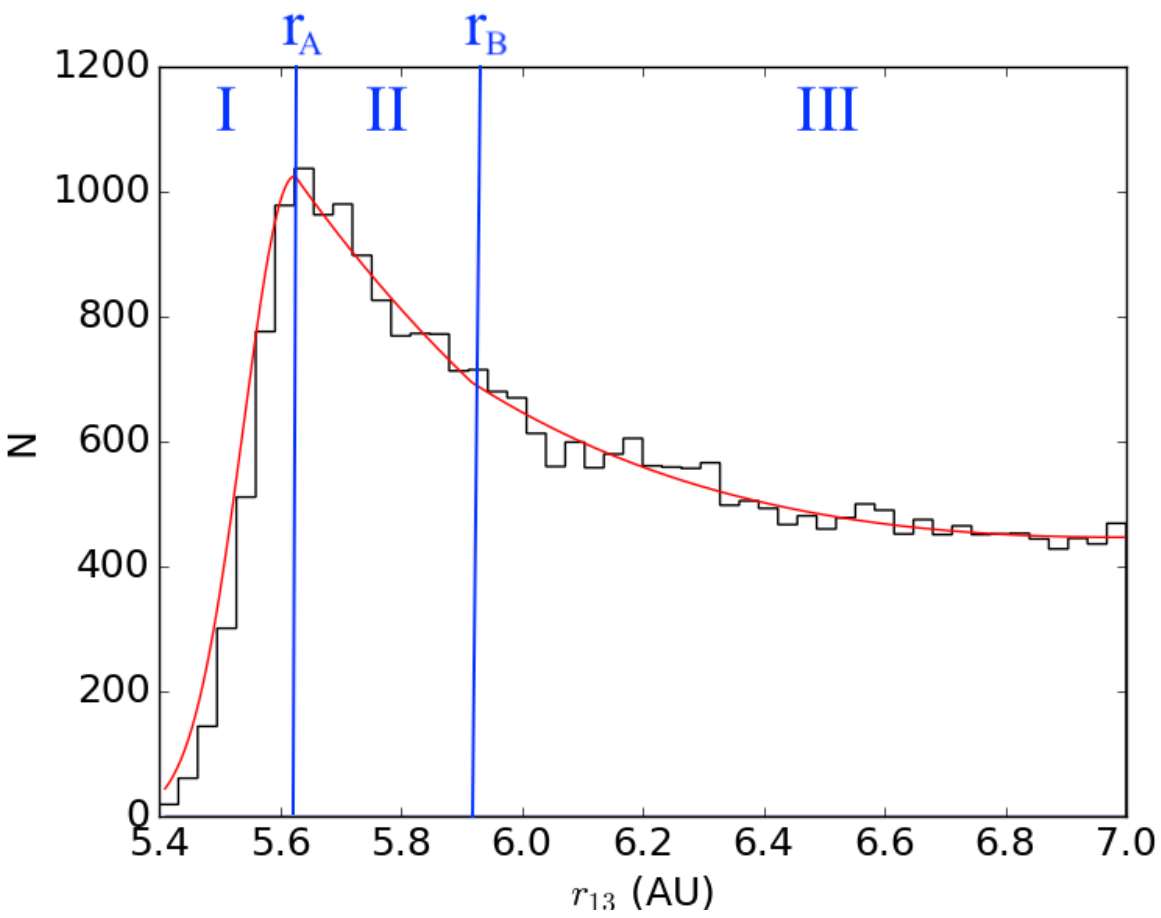

Figure 4.3: Surface density profile (in black) for a system with a 1 $M_\odot$ star and a 10^{-3} $M_\odot$ planet as a function of radius for $\beta = 0.15$. Function fit (in red) to the distribution. There is a sharp inner edge, indicating the existence of a gap in the disc created by the forbidden zone predicted from the restricted three-body problem. There is a more shallow decline at large distances caused by dust grains taking their time spiraling out of the system due to stellar radiation pressure. The characteristic lengths of the gaussian and exponential fits allow us to quantify the width of the ring. These width measurements can be compared to observations since only the brightest, densest regions would be observable. For this particular value of $\beta = 0.15$, we find the normalized ring width to be $\frac{\Delta R}{R} = 0.148\ ^{+0.023}_{-0.025}$, thus meeting the criterion for a thin ring.

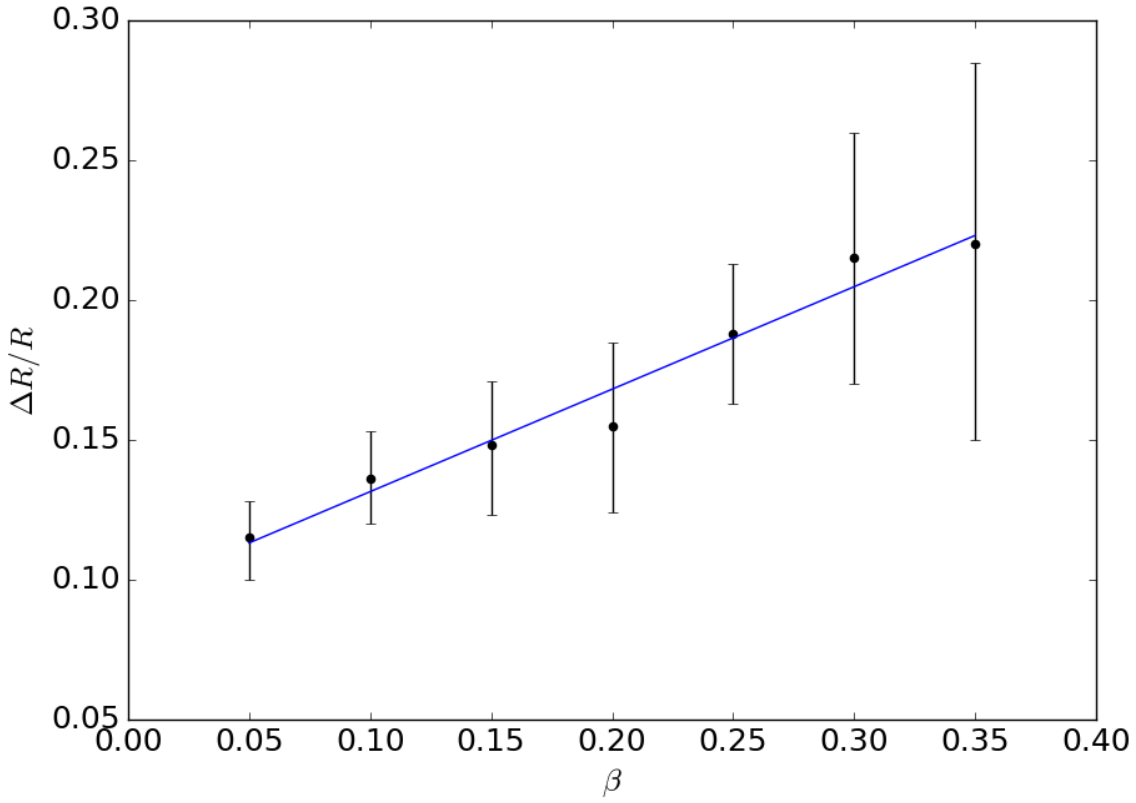

Figure 4.4: Normalized ring widths ($\Delta R/R$) for various values of β for a system with a 1 $M_\odot$ star and a 10^{-3} $M_\odot$ planet . The general trend points to broader ring widths and therefore shallower dropoffs for higher values of β. This is not surprising since higher values of β correspond to stronger radiation pressure. Thus, broader ring widths show dust grains that are actively spiraling out of the system. We also note that the error bars tend to be larger for larger values of β. This is also not surprising since these discs tend to have smaller sample sizes by the end of a controlled simulation, since the stronger radiation pressure ejects a higher percentage of grains from the system.

truncated by the Hill sphere residence time, as shown in Fig. 3.1. The slope of the fiducial $\beta = 0.1$ ISDD is characterized in Fig. 4.5. While the data plotted is from 0 to 100 au, we calculated the slope only for the portion between 5 and 80 au. The characteristic length came out to be 13.7 au, several times the planet semi-major axis, indicating a relatively slow drop-off.

4.5 ISDDs Exhibit a Toroidal Shape

We examined the vertical structure of the simulated disc in addition to the radial structure. Specifically, we plotted the dust grain abundance as a function of height z above or below the midplane of the disc, as seen in Fig. 4.6. In addition, we fit a standard gaussian function to the vertical distribution since the standard deviation would naturally translate to a scale height. We find that the scale height of $H = 0.78$ au for the $\beta = 0.1$ toy model is comparable to both the ring thickness ($\Delta R = 0.64$ au) and Hill radius ($R_{\mathrm{H}} = 0.35$ au).

We attribute the sharp inner edge of the torus to the forbidden zone predicted by the Jacobi constant. Recall from Fig. 2.2 that particles of a certain Jacobi constant are not allowed to exist in certain spaces in the restricted three-body problem. For physically relevant values of β, this region takes the shape of an annulus along the orbit of the planet, approximately one Hill diameter in width. The inner edge of our ISDD represents dust grains bouncing around the edges of the forbidden zone.

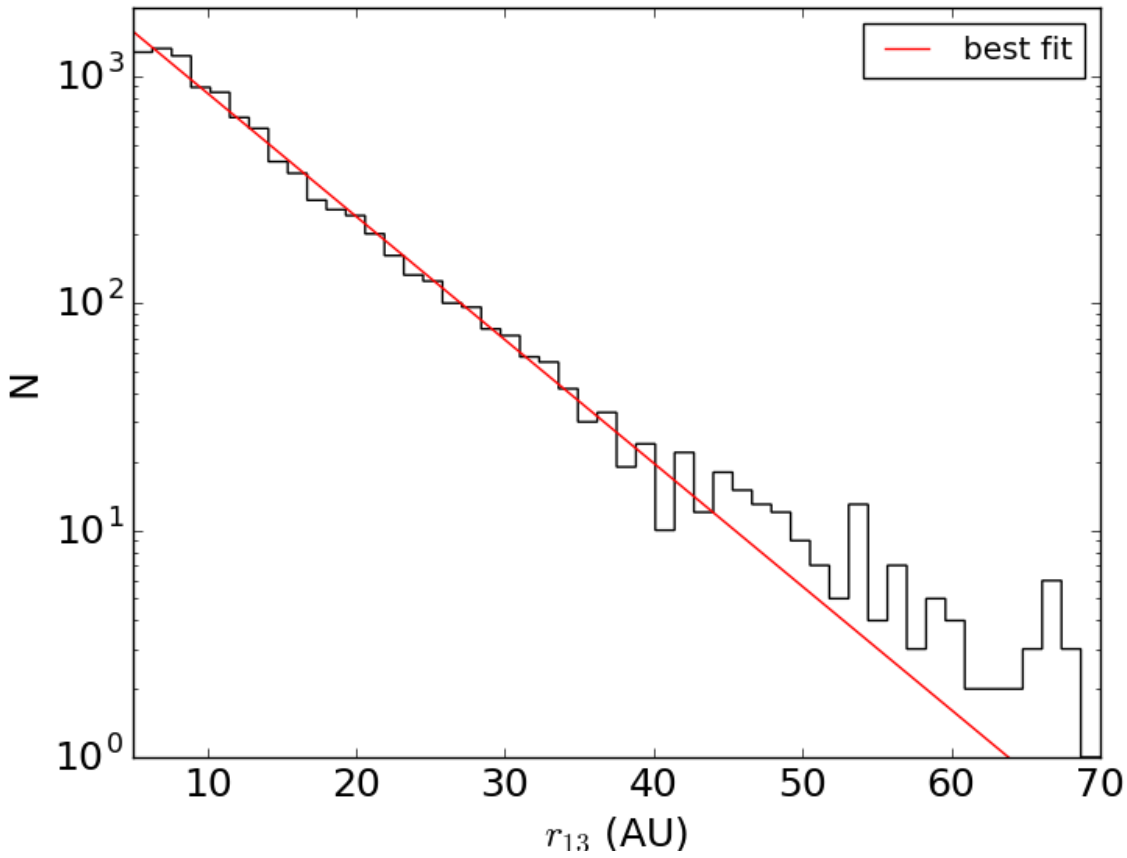

Figure 4.5: Semilog radial profile of fiducial ISDD for $\beta = 0.1$ showing the entire disc from 5 to 70 au. An exponential decay function was fit to the portion of the data from 5 to 70 au to determine the characteristic length of the decay. We find that the profile has a characteristic decay scale of 8.0 au.

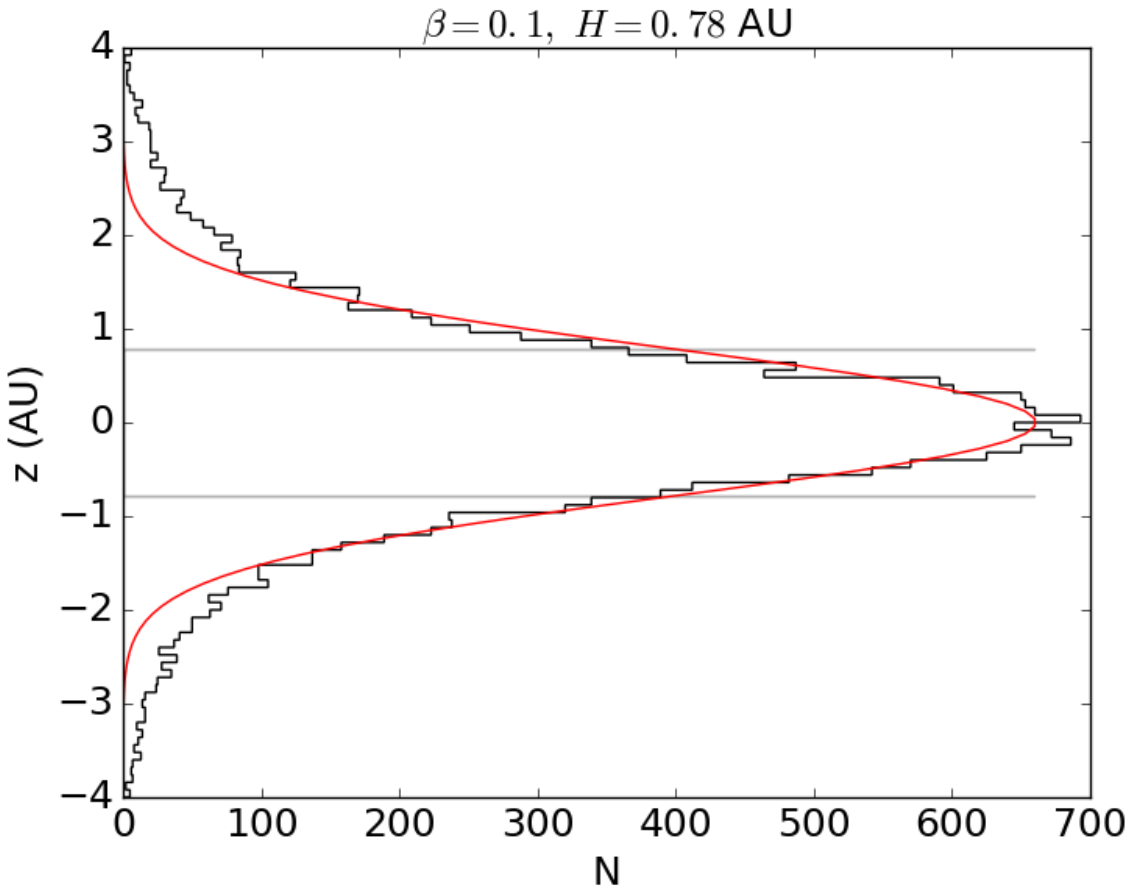

Figure 4.6: Distribution of dust grains as a function of height z. A gaussian function (in red) has been fit to the distribution. The gray horizontal lines represent one scale height (H = 0.78 au) above and below the midplane.

CHAPTER 5

Comparison to Observations

One motivation for this study is the presence of narrow ring-like structures in some observed debris disc systems. The narrowness of the images implies a mechanism for confining either the dust or its parent population. In our model, this is a consequence of the orbital evolution regulated by the Jacobi constant, which sets a hard inner edge on the distribution. The outer profile is more gradual as the dust spirals out, and we compare here this theoretical expectation to properties of the best quantified observed systems.

5.1 Fomalhaut

The existence of a circumstellar disc around the 440 Myr old A3V star Fomalhaut has been known for a long time due to the infrared excess in its spectrum. Fomalhaut is one of the best-studied debris discs, due to its distance from Earth being only 7.7 pc and the fact that it is one of the closest systems that is not edge on. The Fomalhaut debris disc was first directly imaged by Kalas et al. (2005) using the Hubble Space Telescope, revealing a sharp inner edge and the central star being offset from the disc. They derived a flux profile for Fomalhaut by fitting a scattered light model of an inclined, optically thin, belt of dust to observational data, as shown in Fig. 5.1. The best-fitting value for the power law profile describing the inner edge of the belt is proportional to $r^{10.9}$ whereas that of the outer belt scales with $r^{-4.6}$. Similarly, when an exponential profile is used, the inner edge is proportional to $\exp(0.08r)$ while the outer edge scales with $\exp(-0.03r)$, where r in in au. They define the inner edge as 120–140 au and the outer edge as 140–158 au.

Since Kalas et al. (2005) did not explicitly measure a ring width for Fomalhaut, we extrapolate one from their distribution by defining Fomalhaut's normalized ring width to be equal to its full width at half maximum (FWHM) divided by the peak. Under this definition, Fomalhaut's flux profile has a ring width of $\Delta R/R = 0.191$, which fits the definition from Hughes et al. (2018) of a 'narrow' ring as one having a normalized ring width $\Delta R/R < 0.5$.

In order to place the Kalas observations within our paradigm, we fit our function to observations of the radial distribution of the data for Fomalhaut obtained by Kalas et al. (2005). In Fig. 5.1, the red data points are the raw data obtained by Hubble Space Telescope observations, the blue curve is the fit performed by Kalas et al. (2005), and the black curve is our function's fit to the same data. If the Fomalhaut debris disc were formed by a hypothetical planet's irregular satellite cloud, we can estimate that planet's semimajor axis by scaling up our simulated system. Specifically, we scale up the simulated system from Fig. 4.3 so that the peak of the simulated disc's radial profile (5.62 au) matches the peak of the Fomalhaut debris disc's radial profile (144 au). Our model predicts that the planet feeding this disc will have a semimajor axis of 133 au. We fit the piecewise function to the radial distribution to characterize both the inner edge and outer edge. However, our inner edge is best described by a single-sided gaussian as opposed to either a power law or an exponential tail. We find that the inner edge has a characteristic length of 2.23 au and that the outer edge has an exponential decay scale of 20.6 au. The inner edge behavior is very similar to what Kalas et al. (2005) found in their fit for Fomalhaut, but our function has a more gently-sloped outer edge than their fit. If we measure the ring width of the Fomalhaut disk, we get $\Delta R/R = 0.215$, not significantly different from that of Kalas et al. (2005). Thus, the observed profile of the Fomalhaut debris disc is well fit by that expected for an ISDD.

In order to physically interpret our model fit to the Fomalhaut observations, we first estimate which value of β, for a single uniform-β debris disc, best corresponds to the parameters derived from our fit. We start by plotting two key parameters, σ_1 and σ_2, as functions of β, as shown in Fig. 5.2. These two parameters were chosen because they directly determine the measured width of the ring. As one can see, both the inner edge characteristic length and outer edge characteristic length

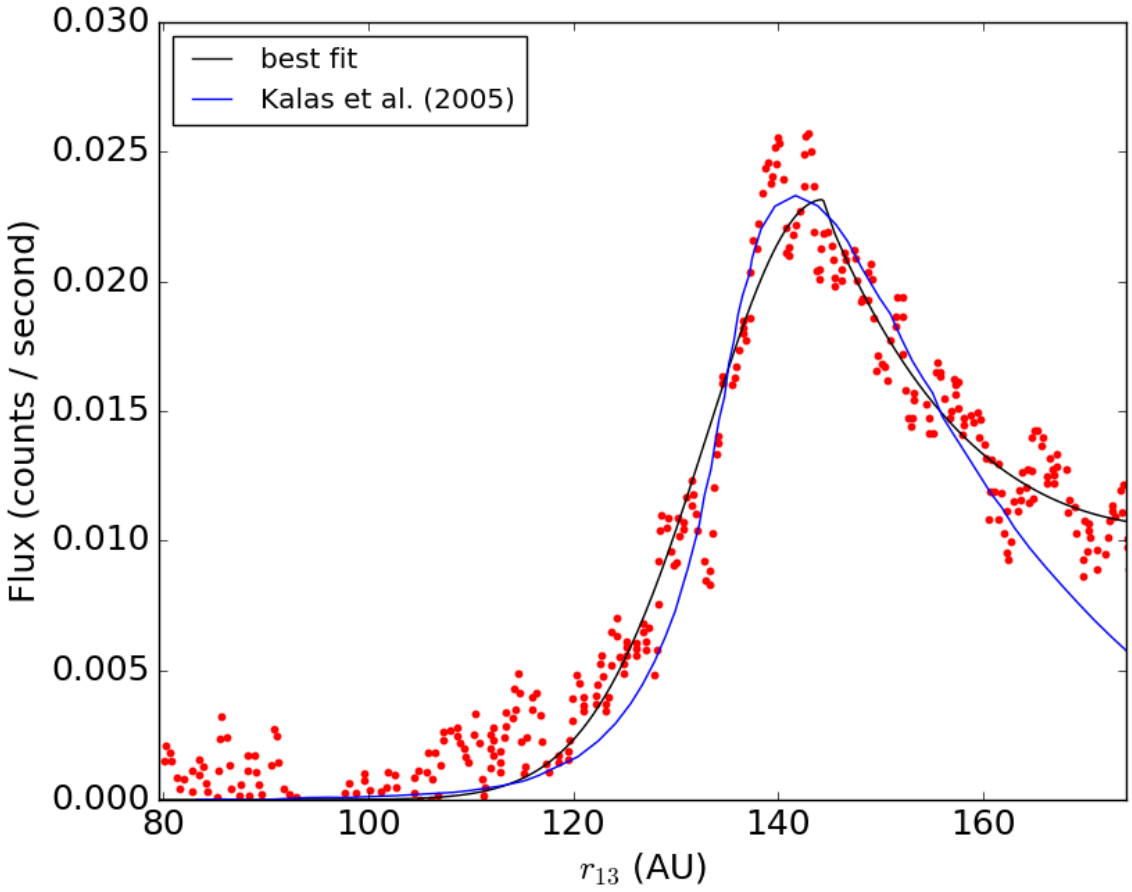

Figure 5.1: Fomalhaut flux profile as a function of radius (Kalas et al. 2005). The inner edge of the belt can be modeled as either a power law fit with an index of $\alpha = 10.9$ or an exponential growth proportional to $\exp(0.08r)$, where r is in units of au. The outer edge of the belt can be modeled as either a power law fit with an index of $\alpha = -4.6$ or an exponential decay proportional to $\exp(-0.03r)$, where r is in units of au. Our model predicts that the planet sculpting this disc will have a semimajor axis of 133 au.

become larger with increasing β. The relatively flat distributions show that our model is quite robust and can replicate Fomalhaut observations for a wide variety of radiation pressure strengths, specifically $\beta \leq 0.3$. This is possible because while there is a very weak dependence of σ_2 on β, σ_1 gets much larger at larger β.

5.1.1 Fomalhaut b

In addition to the debris disc ring, Kalas et al. (2008) also detected a point source that was proposed as Fomalhaut b, a Saturn-mass planet responsible for sculpting the inner edge of the debris disc. In this scenario (Chiang et al. 2009), the planet would have a semi-major axis $\sim$ 115 au and the inner edge of the dust ring would trace the edge of the chaotic region surrounding the planetary orbit. This claim was controversial because the colours of Fomalhaut b showed little evidence for thermal emission from a giant planet, and were far more consistent with pure scattered light from the star. The reality of the source detection itself has been independently confirmed (Currie et al. 2012; Galicher et al. 2013) but further observations by Kalas et al. (2013) reveal several orbital features that make the sculpting planet hypothesis unlikely. The orbit of Fomalhaut b appears to be highly eccentric ($e \sim 0.8$) so that it would cross the debris disc if it were not inclined at $\sim 17°$ to the disc. A planet on such an orbit would be unlikely to gravitationally sculpt the observed structure, as the high eccentricity and nonzero inclination does not correspond to the correct orbital geometry to maintain the original model. Nor is an object on this orbit likely to be the source of an irregular satellite debris disc, at least according to our model, since Kalas et al. (2013) estimates the semimajor axis of Fomalhaut b to be 177 au, much larger than that of the planet we propose, which would be located at 133 au (though their margin of error is quite large at $\pm$68 au).

In order to explain the colours of the original Fomalhaut b hypothetical planet, Kennedy and Wyatt (2011) developed a model starting from a similar hypothesis as ours. They constructed a collisional cascade of irregular satellites within a fraction of the Hill sphere of a giant planet, taking into account the strength versus self-gravity of the satellite. They took into account both radiation pressure and Poynting-Robertson (PR) drag for the resulting dust grains. Kennedy and Wyatt

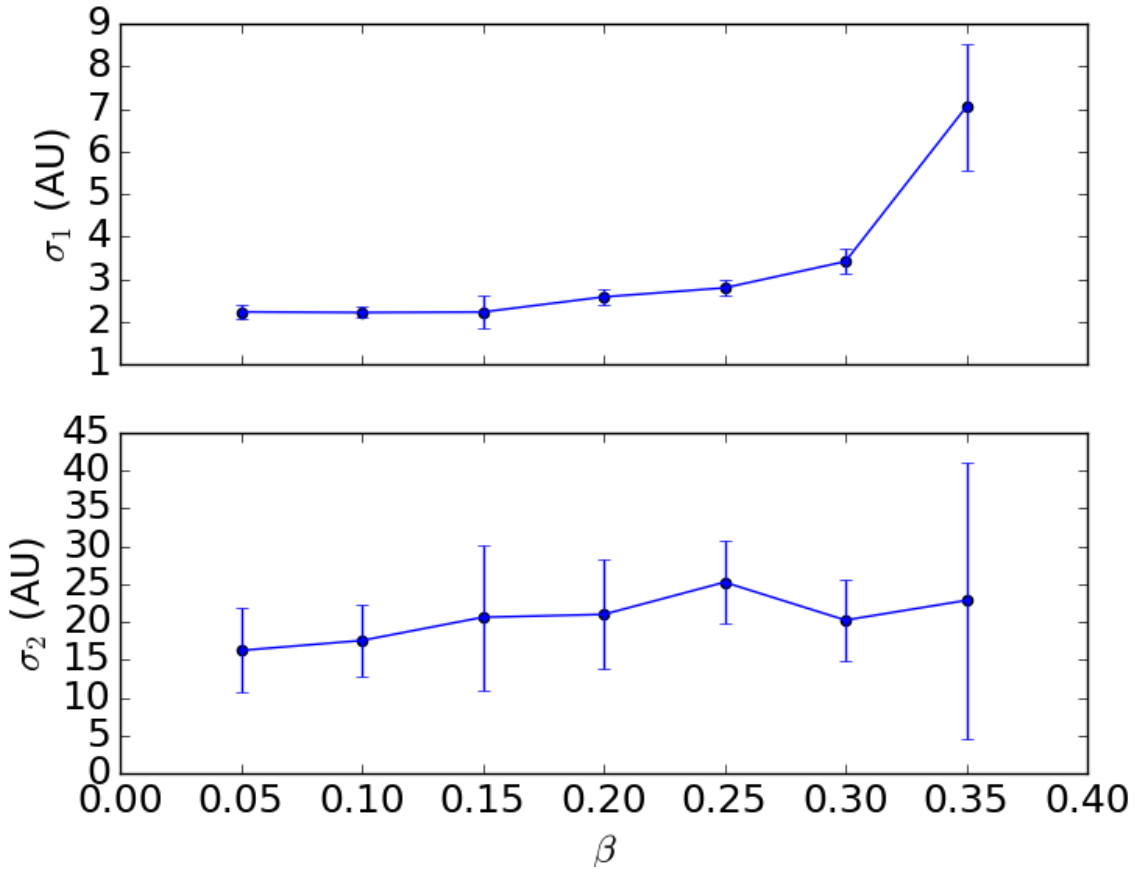

Figure 5.2: Inner edge characteristic length and outer edge characteristic length as functions of β. As expected, both have generally increasing lengths with increasing β, since stronger radiation pressure tends to have a broadening effect on the peak of the distribution. The data begins to become unreliable and noisy at $\beta = 0.35$ due to a small surviving sample size.

(2011) focussed on the appearance of dust confined within the Hill sphere, as a source population for the scattered light observed from Fomalhaut b. In our model, we focus on the dust that has escaped into heliocentric orbit, as the origin of the debris disc itself – not the point source.

5.2 HR 4796A

HR 4796A is an 8 Myr old A0V star that hosts a well-studied debris disc at a distance of 72.8 pc from Earth. The disc has an exceptionally high infrared excess of $f = L_{\rm IR}/L_* = 4.2 \times 10^{-3}$ (Jura 1991). HR 4796A has been imaged in multiple wavelengths including the sub-mm, the mm, mid-infrared, near-infrared, and visible. Combining these different wavelength regimes permits extensive modelling of the spectral energy distribution (SED) of the system. A complete understanding of the SED leads to understanding of the underlying dust composition of the disc. Previous studies have resolved a circular disc structure with a radius of $\sim$ 77 au, with a sharply peaked radial profile, and a $\sim$ 1 au offset from the location of the star. We can learn more about the dynamics of the system from detailed modeling of the exact geometry.

5.2.1 HR 4796A Ring Width

In 2009, the Hubble Space Telescope resolved the debris disc around HR 4796A and found that it has a ring width of 18.5 au and a radius of 76 au (Schneider et al. 2009). Thus, its normalized ring thickness is $\Delta R/R = 0.25$, comparable to that of Fomalhaut and our simulated disc. All three are well within the definition of Hughes et al. (2018) for a narrow ring.

We compare our model to observations of HR 4796A made by Schneider et al. (2009) using the Hubble Space Telescope Imaging Spectrograph. Specifically, we fit our three-regime piecewise function to the intensity profile for a direct one-to-one comparison and extract a normalized ring width, as shown in Fig. 5.3. If the HR 4796A debris disc were formed by a hypothetical planet's irregular satellite cloud, we can estimate that planet's semimajor axis by scaling up our simulated system. Specifically, we scale up the simulated system from Fig. 4.3 so that the peak of the

simulated disc's radial profile (5.62 au) matches the peak of the HR 4796A debris disc's radial profile (76.5 au). Our model predicts that the planet feeding this disc will have a semimajor axis of 70.8 au. We find that our function does an overall good job of fitting the inner edge of the disc, but falls to zero more quickly than the HST data. Mathematically, our function drops to zero quickly since the inner edge is defined by a single-sided gaussian. The discrepancy may be due to background noise in the HST data. As for the outer edge, our function initially drops off a little bit more quickly than the HST data. As a result, the normalized ring width is slightly lower than that derived from the HST observations, but there is not a significant difference. We once again used the full width at half maximum (FWHM) of the radial profile method for determining ring width and find that the ring with for HR 4796A is $\Delta R/R = 18.3$ per cent. We note that HR 4796A, Fomalhaut, and our simulated disc all fall within the definition of a 'thin ring' as defined by Hughes et al. (2018).

5.2.2 HR 4796A Blowout Size

Previous models have argued for a large minimum particle size in the HR 4796A system, and our model supports this claim (e.g., Chen et al. 2020; Milli et al. 2017). We can calculate the dust grain size corresponding to $\beta = 0.1$ for the stellar parameters of HR 4796A, namely the luminosity of 23 $L_\odot$ and mass of 2.18 $M_\odot$, using Equation 2.3. This specific value of β was chosen because it fulfills the criterion laid out in Appendix A to ensure overflow through the L_2 Lagrange point. Rearranging Equation 2.3 to solve for the blowout size $D_{\rm bl}$, we obtain

$$D_{\rm bl} \approx (21.4\ \mu{\rm m})\left(\frac{\beta}{0.1}\right)^{-1}\left(\frac{L_*}{23\ L_\odot}\right)\left(\frac{M_*}{2.18\ M_\odot}\right)^{-1}. \tag{5.1}$$

The result gives us a rather large dust grain diameter of $D \approx 21.4\ \mu$m. Chen et al. (2020) derived a similar minimum grain size of 25 μm by using MCFOST on SPHERE SPF data. Milli et al. (2017) found the grain size range 17.8–30 μm fit the data depending on the exact scattering model used.

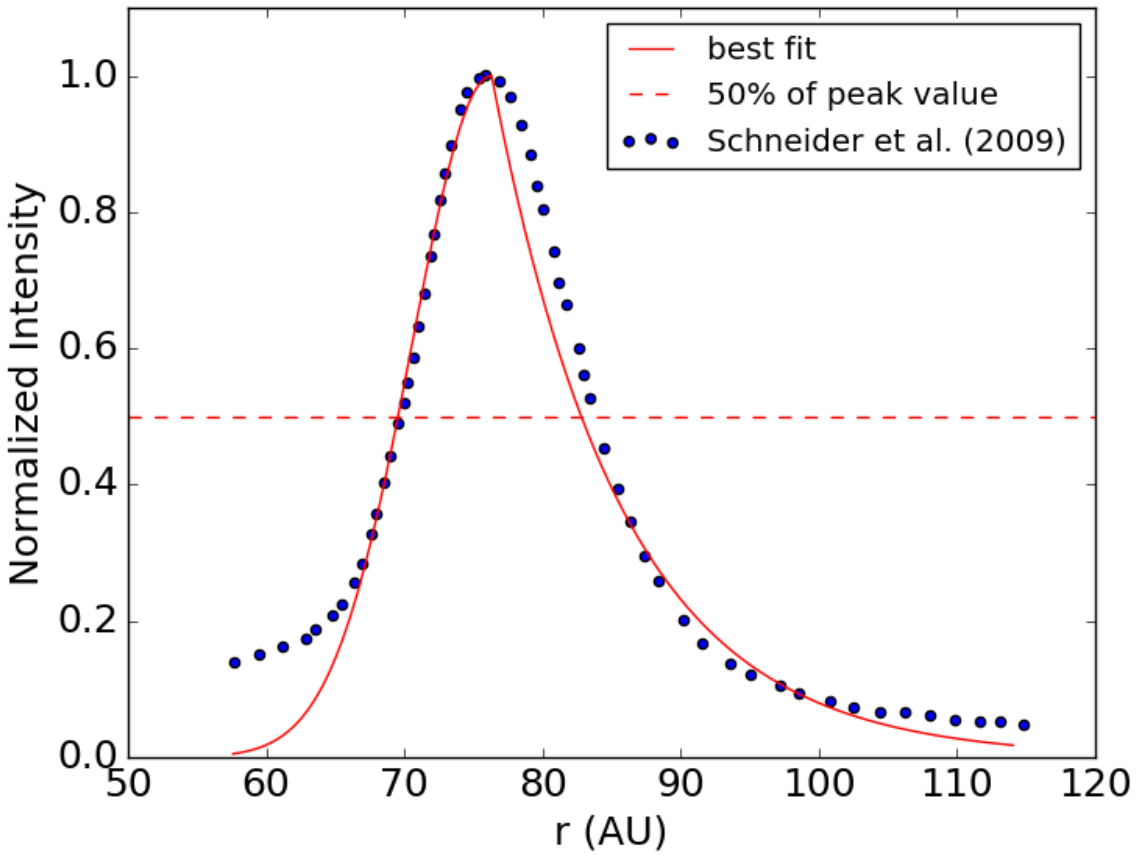

Figure 5.3: The best fit of our three-regime piecewise function fitted to an HR 4796A flux profile from Schneider et al. (2009). A dashed red line is plotted to indicate 50 per cent of the peak value to help visualize the FWHM. We find that the normalized ring width of the system is $\Delta R/R = 18.3$ per cent. Our model predicts that the planet sculpting this disc will have a semimajor axis of 70.8 au.

Division name	Wavelength	β
Mid-wavelength infrared	3 - 8 μm	0.21 - 0.55
Long-wavelength infrared	8 - 15 μm	0.11 - 0.21
Far infrared	15 μm - 1 mm	0.002 - 0.11

Table 5.1: Summary of correspondence between observing wavelength and relative strength of radiation pressure β.

A general rule of thumb states that dust grains are best observed in electromagnetic radiation at wavelengths that are approximately equal to their size (e.g., Hughes et al. 2018). This phenomenon can be explained as a balance between two opposing processes. We first consider the fact that the smallest grains dominate the grain size distribution and thus contribute the most to the total cross section. However, there is a competing effect where grains can only efficiently emit at wavelengths that are smaller than their actual size. A sharp cutoff in this emission efficiency occurs at larger wavelengths. All in all, the total light emitted will receive contributions from the smallest grains that are able to efficiently emit from that wavelength. The observing wavelengths versus β are highlighted in Table 5.1. Although debris discs are typically detected using IR excesses, we are interested in comparing our simulated discs to scattered light images since IR excesses do not give us a geometric picture. Imaging capabilities can vary strongly amongst the different bands in Table 5.1.

The ISDD model offers a natural qualitative explanation for the narrowness of some observed debris discs. Let us therefore compare the quantitative features of the model with the two of the best-studied examples of this class of object: Fomalhaut and HR 4796A.

5.3 Dependence on Planet Mass

Generally speaking, we expect the morphologies of ISDDs to depend on the ratio of planet mass to stellar mass $M_{\rm p}/M_*$. This dependence arises because the Jacobi contours of the restricted

three-body problem depend only on the ratio of the masses of the secondary body to the primary body M_2/M_1, both with and without radiation pressure. For example, a Saturn-like planet orbiting around an M dwarf could have the same normalized Jacobi contours as a Jupiter-like planet orbiting around a G-type star.

Since the thickness of the Jacobi forbidden zone is roughly the same size as the diameter of the Hill sphere, we expect any ensuing ring gaps to be a similar size to the Hill diameter as well. This effect would likely only be noticeable in low radiation pressure scenarios, since those are the only cases where a significant number of dust grains escape interior to the planet's orbit and would therefore produce an observable ring gap in the radial distribution. Appendix B goes into greater detail the theoretical foundation of exactly how the mass ratio correlates with the critical β.

5.4 General Predictions for Other Systems

5.4.1 Wavelength Dependence

Different observing wavelengths will be able to probe different structures of potentially the same debris disc. For example, since observing wavelength is expected to be directly proportional to grain size and therefore inversely proportional to β, we predict that the long-wavelength infrared ($\lambda = 8-15\ \mu$m) will find singular thin rings. Due to the stronger influence of radiation pressure, mid-wavelength infrared ($\lambda = 3-8\ \mu$m) will detect comparatively broader rings than found in the long-wavelength infrared, but still one singular ring. However, in the far infrared ($\lambda = 15\ \mu\text{m} - 1\ mm$), which can be affected by values of β as low as 0.002, we expect there to be a gap in the ring since Roche lobe overflow through the L_1 Lagrange point is almost equally favorable to occur energetically. In this instance, dust escapes both inward and outward through L_1 and L_2, but the Jacobi forbidden zone prevents the two populations from mixing, giving rise to the gap in the ring.

5.4.2 Evolutionary Implications

At first glance, irregular satellite collisions would appear to not explain the debris discs found around such aged systems as Fomalhaut (440 Myr), due to how quickly they grind down to dust and dissipate (~tens to hundreds of thousands of years). Thus, irregular satellite debris discs would only be bright enough to be detectable in their infancy. However, irregular satellites are not formed in the same way as regular satellites, and thus do not have the same age as their host planet. In our own Solar system, they are thought to be the result of dynamical capture during late-stage rearrangement of the giant planet orbits (Nesvorný et al. 2007), hundreds of Myr after the formation of the Solar System. This delay can help us explain the age of older debris disc systems.

The size of the dust in such discs may also be a function of time, because the β of the escaping material is set by the balance between residence and collision times. The latter will increase as the mass reservoir in the source population grinds down, moving the characteristic β of the escaping particles to lower values, and therefore increasing the size of the particles in the disc.

CHAPTER 6

The Effects of Introducing Eccentricity into the Planet's Orbit

In previous chapters, we assumed for simplicity that the orbit of the Jupiter-mass planet is a perfect circle. In other words, the eccentricity is equal to zero. However, even the eight planets in our Solar System, whose orbits are frequently approximated to be perfect circles, have finite eccentricities ranging from $e = 0.007$ for Venus to $e = 0.206$ for Mercury (Murray and Dermott 1999). Moreover, the known exoplanet population exhibits a wider range of orbital eccentricities compared to Solar System planets and has a much higher average eccentricity. In one sample of 403 exoplanets discovered using the radial velocity method, Limbach and Turner (2015) found that the average eccentricity of each planetary systems was anti-correlated with multiplicity, or the number of planets in the system. Specifically, the average eccentricity ranged from $e = 0.27$ for single-planet systems to $e = 0.06$ for octuple-planet systems like our Solar System.

One of our original goals and motivations was to explain the thin, eccentric debris rings that were often found around local A-type stars. We were previously successful in showing that dust generated from collisions between irregular satellites were consistent with observations of thin, circular rings. If circular orbits can give rise to circular rings, then the natural next step is to investigate whether eccentric orbits can give rise to eccentric rings.

One of the core assumptions of the circular restricted three-body problem is that the secondary body (planet) must be on a perfectly circular orbit around the primary body (star). This assumption allowed us to identify a co-rotating frame that spun at a constant rate Ω, the same rate that the planet orbited around the star. Furthermore, a conserved quantity was identified in the circular restricted three-body problem—the Jacobi constant C_J. Having units of energy, the Jacobi constant was an

energy-like quantity that predicted certain regions of space where test particles (dust grains) were and were not allowed to traverse. This formalism gave rise to the classical 'forbidden zones' and 'allowed zones' of the Jacobi constant. The forbidden zone was typically a horseshoe- or even annulus-shaped contour with a radius approximately equal to the planet's semimajor axis and a width approximately equal to the planet's Hill diameter.

Let us first consider systems with a single planet on a low eccentricity orbit. Thus, we can approach the problem from a perturbation theory angle, with the small perturbed quantity being eccentricity e. For small enough eccentricities, we would assume that results from the circular restricted three-body problem such as the existence of the Jacobi constant and forbidden zone would generally hold. When eccentricity is pumped too high, we would eventually expect these predictions to break down, showing that our initial assumption of a low eccentricity orbit is no longer valid. The exact breaking point will be determined experimentally through numerical simulations. For the low eccentricities, we can likely expect the forbidden zone to generally hold, and that its shape will generally follow the shape of the orbit. So instead of being a nearly perfect circle, we expect the forbidden zone to warp into an ellipse.

6.1 Hill Sphere Escape Fraction as a Function of Eccentricity and Radiation Pressure Strength β

One starting point for understanding the effect of introducing eccentricity into the planet's orbit is to measure what percentage of dust grains are able to escape from the planet's Hill sphere for a particular eccentricity and β. When dust grains are released in an 'avalanche cascade' fashion, we find that an equilibrium between dust grains exiting the Hill sphere and entering the Hill sphere is reached quite quickly. As a result, we can define Hill sphere escape fraction to be the asymptotic value approached by the end of a $\Delta T = 1,200$ yr simulation. Specifically, the initial positions of such a simulation are originating between $r = 0.3$–$0.4\ R_H$ for radius and in polar coordinates θ and ϕ, $\cos(\theta)$ is distributed uniformly in [-1,1) and ϕ is distributed uniformly in [0,2π). The initial

e	β					
	0	**0.1**	**0.2**	**0.3**	**0.4**	**0.5**
0	0%	0%	15.77%	21.28%	31.61%	48.81%
0.1	0%	0%	0.34%	23.08%	47.31%	71.52%
0.3	1.06%	14.77%	65.46%	83.79%	93.09%	97.43%
0.5	83.20%	84.62%	98.72%	99.58%	99.82%	99.94%
0.7	97.48%	99.47%	99.88%	100%	100%	100%
0.9	99.98%	100%	100%	100%	100%	100%

Table 6.1: Hill sphere escape fraction as a function of eccentricity e and radiation pressure strength β, shaded linearly. Increasing eccentricity or radiation pressure while holding the other constant typically has the effect of increasing the escape fraction. High-eccentricity orbits ($e > 0.5$) have near unity escape fractions regardless of radiation pressure strength.

velocities are set to be 71 per cent of the local keplerian velocity, which was empirically found to be the maximum velocity at which no grains escape from the Hill sphere when $\beta < 0.005$.

The main two quantities that will be varied are the eccentricity of the planet's orbit, e, and the relative radiation pressure strength, β. In order to reasonably probe the entire parameter space between e and β, we have chosen the following representative values: $e = 0, 0.1, 0.3, 0.5, 0.7, 0.9$ and $\beta = 0, 0.1, 0.2, 0.3, 0.4, 0.5$. Probing $\beta > 0.5$ is not necessary since $\beta = 0.5$ is the canonical blowout size where dust grains are able to escape the gravitational field of the star (Krivov 2010). Results are summarized in Table 6.1.

Generally speaking, increasing either eccentricity or β while holding the other quantity constant has the effect of increasing escape fraction. Eccentricity has a stronger effect on escape fraction than β, with all simulations of eccentricity $e \geq 0.5$ achieving escape fractions greater than 83 per cent. On the other hand, maxing out β at 0.5 while keeping in eccentricity at zero results in an escape fraction of only 49 per cent.

Several combinations of eccentricity and β are to be ruled out from feasibly forming circum-

stellar disks due to their nearly zero Hill sphere escape fractions. They tend to be clustered near the upper-left of Table 6.1 where low eccentricity and low radiation pressure intersect. These simulations will be kept in mind in the next section's analysis and denoted by 'N/A' in Table 6.2.

6.2 Disk Lifetime as a Function of Eccentricity and Radiation Pressure Strength β

In order to characterize the lifetime of a disk for a particular planetary orbit eccentricity e and radiation pressure strength β, we employ an 'avalanche cascade' model as opposed to a 'collisional cascade' one. In an avalanche cascade, all of the dust grains are generated and released at the very beginning of the numerical simulation. On the other hand, in a collisional cascade, the dust grains are assumed to be continuously generated and slowly released into the system over time at a rate that can vary or be constant. We believe that an avalanche cascade is more appropriate for the goal of measuring disk lifetime.

We begin by defining 'disk lifetime' to be the amount of time it takes for the maximum number of dust grains that escape from the Hill sphere N_{esc} to drop to $1/e$ of its original value. In general, there are three mechanisms that a dust grain can be 'lost' from the system: (1) collision with the central star, (2) collision with the planet, or (3) ejection beyond the edge of the system, which is defined to be 100 au for simplicity. We discuss in Appendix C why collisions between circumstellar dust grains are ignored. However, in practice, only mechanism (3) matters for the purpose of calculating disk lifetime. Mechanism (1) does not occur because dust grains can only escape exterior to the planet's orbit through the L_2 Lagrange point in our simulations. Furthermore, mechanism (2) cannot occur by default since the definition of disk lifetime only takes into account dust grains that successfully exit the Hill sphere.

Results are summarized in Table 6.2. Generally speaking, increasing either eccentricity or β while holding the other constant has the effect of decreasing the disk lifetime. For β, this behavior is quite intuitive since increased radiation pressure will make it easier for dust grains to escape from

e	β					
	0	**0.1**	**0.2**	**0.3**	**0.4**	**0.5**
0	N/A	N/A	33,600	15,000	7,440	38
0.1	N/A	N/A	N/A	21,600	9,480	37
0.3	N/A	54,000	36,600	6,120	75	54
0.5	142,429	64,800	5,460	66	45	36
0.7	53,400	12,588	26	11	9	7
0.9	8,460	23	8	4	2.5	1

Table 6.2: Disk lifetime (in years) as a function of eccentricity e and radiation pressure strength β, shaded logarithmically. We define disk lifetime as the time (if any) it takes for the number of grains that escape from the Hill sphere N_{esc} to drop to $1/e$ of the maximum value. Disk lifetimes for certain combinations of low eccentricity and/or low β were not obtainable (denoted by 'N/A' and shaded red) due to insufficient Hill sphere escape fractions (see Table 6.1).

the star's gravitational field. Increased planetary eccentricity has a somewhat similar effect since dust grains will also start on more eccentric orbits, making it easier for them to escape to the 100 au limit we have set up in our simulations.

A clear diagonal trend appears in our parameter space exploration, showing that a moderate amount of eccentricity and β are required to produce long-lived ring structures. If both eccentricity and β are too high, then all of the dust grains will be liberated from the Hill sphere quickly and escape to infinity in under 100 years. On the other hand, if both eccentricity and β are too small, then none of the dust grains will escape from the Hill sphere and there is no circumstellar disk. However, these systems will continue to evolve. Since a collisional cascade is actively occurring in the background, these systems will undergo further grinding to small dust grains, effectively moving rightward in Table 6.2 until they reach a suitable combination of eccentricity and β to form a long-lived circumstellar disk.

6.3 Results

Now that we have identified a set of interesting combinations of eccentricity and β and denoted by the diagonal in Table 6.2, we can create scatter plots of the steady-state configurations that these disks approach. Specifically, we plot in Figure 6.1 six disks from the six representative values of eccentricity (0, 0.1, 0.3, 0.5, 0.7, 0.9) after $\Delta T = 1,200$ year simulations. Several notable trends occur:

- Eccentric inner edge—the shape of the ring's inner edge (and underlying forbidden zone) matches the shape of the planet's orbit.
- Asymmetric ring arcs—in moderate eccentricity disks ($e = 0.3$–0.5), there is a noticeable arc-shaped overdensity in dust grains in the vicinity of the planet's position in the orbit.
- Increasing escape fraction—more dust grains escape as eccentricity is increased for a fixed β.
- Parabolic outer edge—outer edge of disk is a parabola with a vertex roughly aligned with the elliptical orbit's pericenter.
- Asymmetric escape cycle—dust grains escape more easily in the portion of the orbit from pericenter to apocenter (planet decelerating) than from apocenter to pericenter (planet accelerating).

In the low eccentricity case ($e \lesssim 0.5$), the shape of the forbidden zone and ensuing inner edge indeed warps into that of an ellipse. This trend generally holds even as eccentricity is pumped to moderate values ($e \approx 0.5$). However, the rigor of the forbidden zone clearly break down at high eccentricities ($e \gtrsim 0.7$) as a significant number of dust grains are able to escape interior to the planet's orbit.

We observed previously in Table 6.1 that a higher percentage of dust grains are able to escape from the Hill sphere as eccentricity is increased while holding β constant.

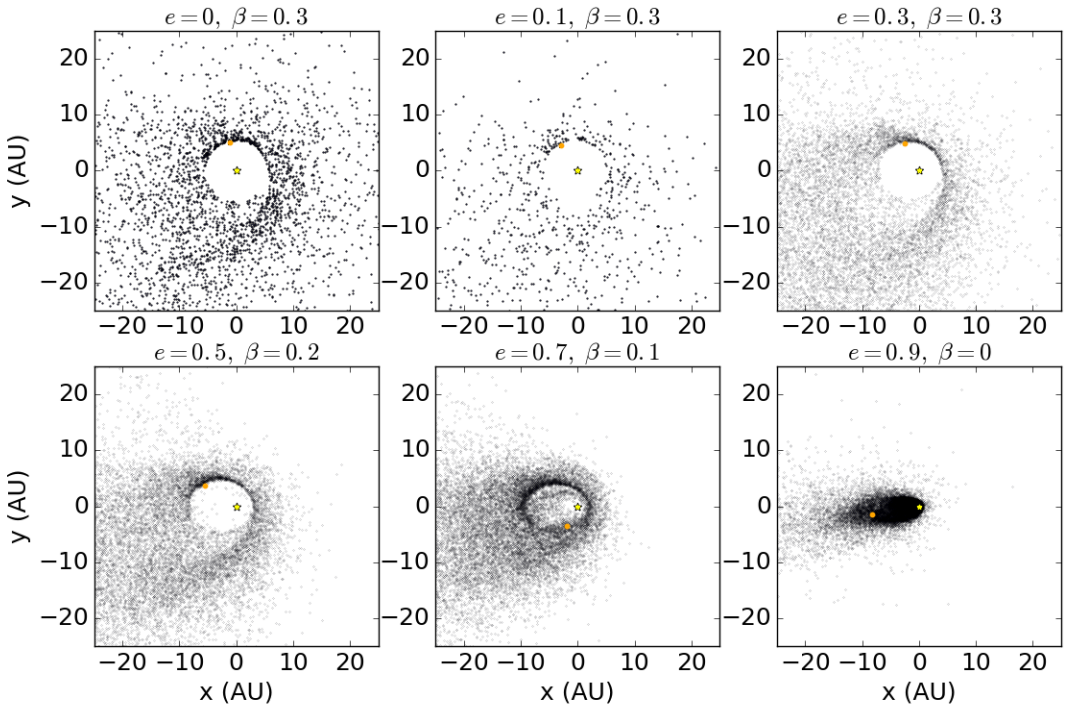

Figure 6.1: Scatter plots of dust grains for increasing planetary eccentricity, e. Periapse is always located along the x-axis to the right of the star for consistency purposes. Appropriate values of β were chosen for each eccentricity such that nonzero Hill sphere escape fractions were achieved in addition to long-lived steady-state disks, based on results from Tables 6.1 and 6.2. Note that the location of the star relative to the disk is an indicator of eccentricity since the star must be at the focus of an elliptical orbit.

The observations of a parabolic outer edge and asymmetric escape cycle are linked to one another. Dust grains are able to escape more easily from the Hill sphere while the planet is decelerating in its orbit due to the shift in relative velocity. This preferred timing cause the pericenters of the individual dust grains' elliptical orbits to align with the pericenter of the planet's orbit. After the disk has had time to smooth out and reach a steady state, this alignment of pericenters has the overall effect of creating a parabolic-shaped outer edge of the disk since the closest approaches of all objects occur on the same side of the orbits.

In summary, we have shown that introducing eccentricity into the planet's orbit yields eccentric disks for low to moderate eccentricities ($e \leq 0.5$). In addition, these dust distributions produce asymmetries which could make it possible to distinguish these systems from others observationally. Specifically, the ring arcs and parabolic outer edge are asymmetric observational signatures of dust produced by collisions between the irregular satellites of a planet on an eccentric orbit.

CHAPTER 7

Conclusions

In this paper, we explored the effects of including radiation pressure into the classical restricted three-body problem. We found that the traditional Roche lobe overflow can be replaced by Lagrange point L_2 overflow for a sufficiently high β for a given planet-to-star mass ratio μ_2/μ_1. Sample orbital integrations reveal that individual dust grains typically trace out 'flower petal' orbits, coming to rest on the zero-velocity curves for some time.

We assumed that the origin of dust grains in our model were from collisions between the giant planet's irregular satellites. We motivated our initial conditions based off of observations of the Solar System giant planets' irregular satellites today as well as what previous studies' determined from their dynamical history. We describe the size distribution of bodies ensuing from irregular satellite collisions as a collisional cascade power law distribution. We calculate the catastrophic collisional time-scale and compare it to an empirically determined residence time-scale to determine the critical β at which ground down dust grains can escape the Hill sphere.

Our N-body simulations show that dust grains with a β above $\beta_{\rm crit}$ quickly escape from the Hill sphere and transition from a circumplanetary orbit to a circumstellar orbit. After a short time, a large population of dust grains achieve an azimuthally symmetric disc appearance. We evaluated this azimuthal symmetry by comparing the fluctuations in the azimuthal profile to the average column density and found that they were low. We also calculated the average radius along a given azimuthal angle θ and found that the mean and median radius is consistent along all azimuthal angles.

We fit a piecewise function with an gaussian inner edge and exponential outer edge to the radial

profile. These functions naturally allowed us to quantify the ring width for various values of β. We normalized the ring width over the ring radius as is standard in the literature ($\Delta R/R$), and find that normalized ring width broadens as a function of β. We explain this finding as stronger radiation pressure being able to excite dust grains to more eccentric orbits and therefore broadening the overall distribution. Since the vertical profile of the disc resembles a typically gaussian, we conclude that the overall shape of the disc is a torus.

We compared our results to observations for the specific systems of Fomalhaut and HR 4796A, but also make general predictions for all systems. For the assumption of uniform density spherical dust grains, there is an inverse relationship between observing wavelength and β. We find that the topology of the debris disc is dictated by the original Jacobi forbidden zone contours, so the fundamental parameter is the planet-to-star mass ratio M_2/M_1.

We test the validity of our radial profile fitting function by applying it to the raw Hubble Space Telescope data of Fomalhaut from Kalas et al. (2005). We obtain very similar results to their fit in terms of inner and outer edge slopes. By defining a ring width for Fomalhaut as its full width at half maximum, we measure its normalized ring width to be 0.191, comparable to our model's $\Delta R/R = 0.13$, both of which are within the 'thin ring' definition defined in Hughes et al. (2018) of $\Delta R/R = 0.20$. We note that there is an ongoing debate about whether Fomalhaut b is a planet or a transient dust cloud and clarify that due to its inclined orbital plane with respect to the disc plane, we do not assume Fomalhaut b is the source of the debris disc in our model, but rather some other underlying hidden planet.

For the assumption of a Sun-like star, we make general predictions about distinctions between observing wavelengths in the mid-wavelength infrared, long-wavelength infrared, and far infrared. We address the fact that while irregular satellite swarms tend to grind down very quickly on time-scales of tens to hundreds of thousands of years, they can still explain very old systems such as Fomalhaut since irregular satellites were not expected to be captured until the Late Heavy Bombardment period in our Solar System.

Lastly, we varied the eccentricity of the Jupiter-mass planet to investigate the ensuing effects

on the morphology of the disk. We narrowed down the parameter space of all physically relevant combinations of eccentricity and β that produce circumstellar disks. Specifically, we first measured the Hill sphere escape fractions of three dozen simulated disks that each contained representative values of eccentricity and β. Second, we measured the disk lifetimes to rule out any systems that eject their dust grains on too short of a timescale ($< 1,000 years$). These two criteria allowed us to identify a diagonal in Table 6.2 of interesting combinations of eccentricity and β that give rise to long-lived circumstellar disks. In other words, only combinations of eccentricity and β that add up to a moderate value are in the sweet spot for liberating dust grains from the Hill sphere, but not so strong that they immediately expel the grains from the system altogether.

After identifying this critical diagonal region, we made five observational signatures of these systems: (1) an eccentric inner edge that follows an eccentric forbidden zone, (2) asymmetric ring arcs near the planet's position in the orbit, (3) increasing escape fraction as a function of eccentricity, (4) a parabolic outer edge with a vertex roughly aligned with the elliptical orbit's pericenter, and (5) an asymmetric escape cycle where dust grains escape from the Hill sphere more easily between pericenter and apocenter.

APPENDIX A

Critical Value for L_1/L_2 Crossover

In the limit of $\beta = 0$, the lowest energy threshold for mass loss from the planetary Hill sphere is through the L_1 point, but this switches to the L_2 point if β is large enough. We wish to quantify the nature of this transition. We will follow the notation of Murray and Dermott (1999).

In the traditional description of the restricted three-body problem, we define a co-ordinate system co-rotating with two massive bodies, of masses μ_1 and μ_2, such that $\mu_1 + \mu_2 = 1$. If we further normalise the angular rotation $n = 1$ and designate the x-axis as the one upon which the massive bodies lie, then the dynamical equations to describe the motion of a test particle in this frame are

$$\ddot{x} - 2\dot{y} - x = -\left[\mu_1(1-\beta)\frac{(x+\mu_2)}{r_1^3} + \mu_2\frac{(x-\mu_1}{r_2^3}\right] \tag{A.1}$$

$$\ddot{y} + 2\dot{x} - y = -\left[\mu_1(1-\beta)\frac{y}{r_1^3} + \mu_2\frac{y}{r_2^3}\right] \tag{A.2}$$

$$\ddot{z} = -\left[\mu_1(1-\beta)\frac{z}{r_1^3} + \mu_2\frac{z}{r_2^3}\right] \tag{A.3}$$

where the massive particles are located at $x = -\mu_2$ and $x = \mu_1$ respectively. As in the case where we ignore radiation pressure, the dynamics are regulated by a pseudopotential, which takes the form (in the $z = 0$ plane)

$$U = \mu_1\left[\frac{1}{2}r_1^2 + \frac{1-\beta}{r_1}\right] + \mu_2\left[\frac{1}{2}r_2^2 + \frac{1}{r_2}\right] - \frac{1}{2}\mu_1\mu_2 \tag{A.4}$$

The equilibrium points are to be found at the extrema of this potential. The criterion for the L_1

point can be written as

$$\alpha^3 = r_2^3 \frac{\left[1 - r_2 + \frac{1}{3}r_2^2 - \frac{\beta}{3r_2}\right]}{(1 + r_2 + r_2^2)(1 - r_2)^3} \tag{A.5}$$

where we have used $r_1 + r_2 = 1$, so $r_1 = x + \mu_2$ and $r_2 = \mu_1 - x$. We have also defined $\alpha = [\mu_2/(3\mu_1)]^{1/3}$. The value of the pseudopotential at this point is

$$\left(\frac{U_1}{\mu_1}\right) = \frac{1}{2}(1 - r_2)^2 + \frac{1 - \beta}{1 - r_2} + 3\alpha^3 \left(\frac{1}{2}r_2^2 + \frac{1}{r_2}\right) - \frac{3}{2}\alpha^3 \tag{A.6}$$

One can develop similar expressions for the L_2 point, where $r_1 = 1 + r_2$, $r_1 = x + \mu_2$ and $r_2 = x - \mu_1$. These are

$$\alpha^3 = r_2^3 \frac{\left[1 + r_2 + \frac{1}{3}r_2^2 - \frac{\beta}{3r_2}\right]}{(1 + r_2)^2(1 - r_2)^3} \tag{A.7}$$

$$\left(\frac{U_2}{\mu_1}\right) = \frac{1}{2}(1 + r_2)^2 + \frac{1 - \beta}{1 + r_2} + 3\alpha^3 \left(\frac{1}{2}r_2^2 + \frac{1}{r_2}\right) - \frac{3}{2}\alpha^3 \tag{A.8}$$

The topology of the Hill sphere changes when $U_1 = U_2$. Fig. A.1 shows this criterion as a function of β and the mass ratio μ_2/μ_1. As the planetary mass increases, it requires stronger radiation pressure to generate an external debris disc.

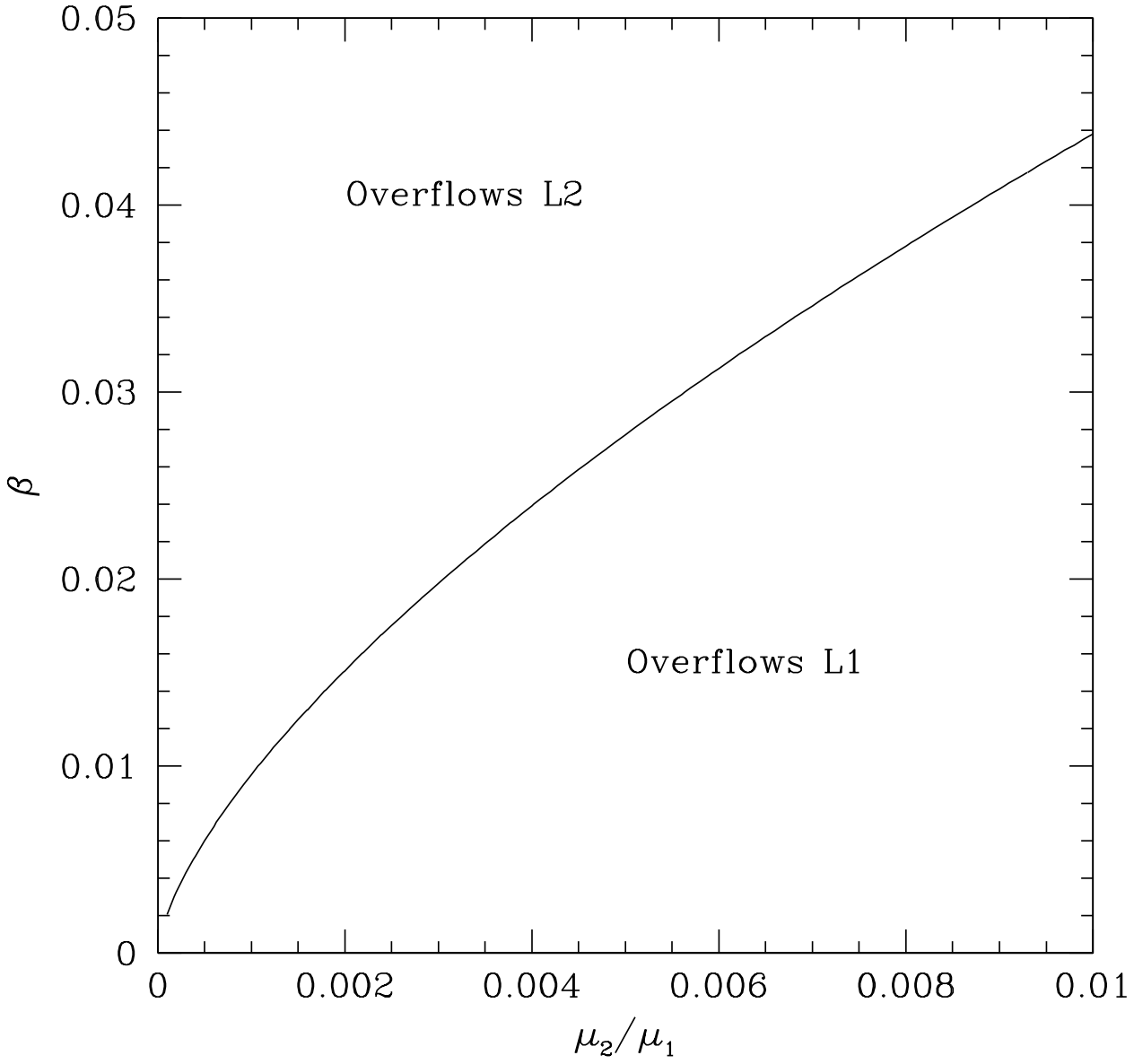

Figure A.1: The curve illustrates the relationship between the radiation pressure strength β and the planetary mass ratio μ_2/μ_1, such that the value of the potential at the L_1 and L_2 points are the same. For values above this curve, dust particles spiral outwards, rather than inwards.

APPENDIX B

Forbidden Zone Thickness as a Function of Radiation Pressure and Mass Ratio

In Section 2.2, we showed one example of how the forbidden zone contours of the restricted three-body problem changes as a function of radiation pressure by comparing and contrasting the zero-velocity curves for $\beta = 0$ and $\beta = 0.1$. As we saw in that section, there were two primary changes in the zero-velocity curves for that example–the forbidden zone thickness increased with radiation pressure, but the radius of both the inner and outer edges shrunk. In other words, the radius of the outer edge of the forbidden zone shrunk by less than that of the inner edge.

In this Appendix, we explore a much more comprehensive range of representative values for radiation pressure strength, β, and allow the mass ratio the vary, as shown in Fig. B.1. We choose a range of $\beta = 0 - 0.5$ since $\beta = 0.5$ is the traditional blow-out point in the restricted two-body problem. For mass ratio, we choose a generous range of $M_2/M_1 = 10^{-6}$ to 1 to explore the effects of radiation pressure from as low as an Earth-to-Sun mass ratio up to all possible binary stellar companions.

The main trend here is that the forbidden zone thickness is much more sensitive to radiation pressure changes for smaller mass ratios. Specifically, small mass ratios are defined as as low as $M_2/M_1 = 10^{-6}$ like for an Earth-Sun relationship, all the way up to $M_2/M_1 = 10^{-3}$, like for a Jupiter-Sun relationship. For mass ratios that approach unity for brown dwarf companions and binary stars, radiation pressure does not have much of an effect on forbidden zone thickness. Lastly, we overplot the chaotic zone width results from Chiang et al. (2009) to show that we obtained a nearly identical slope to them, just with a slightly different amplitude. Their estimate for the width

of the chaotic zone is essentially our upper limit for the width of the forbidden zone, likely due to the fact that we only considered Jacobi constants that originated in the range $0.3R_{\mathrm{H}}$ to $0.5R_{\mathrm{H}}$.

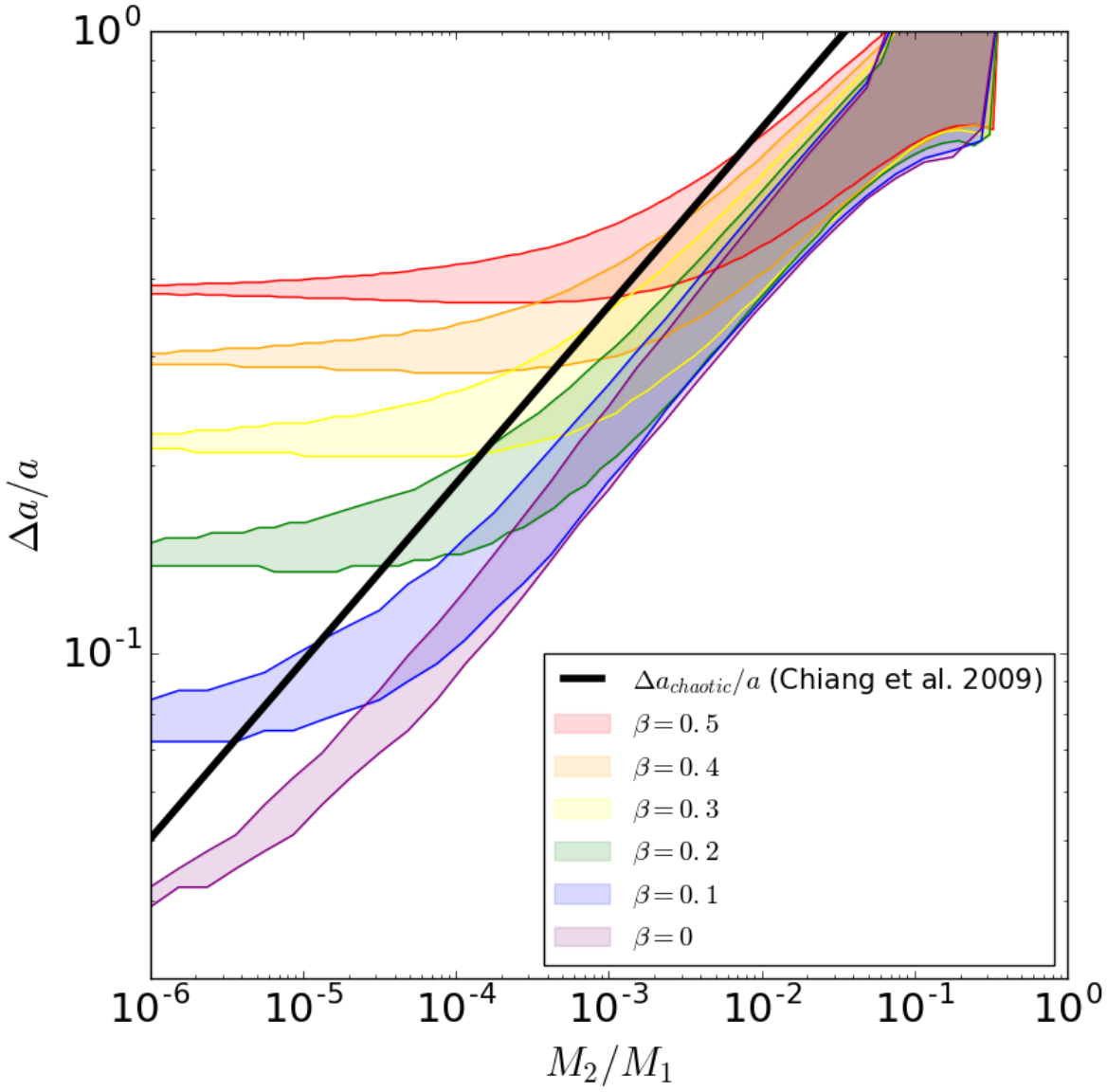

Figure B.1: Normalized forbidden zone thickness ranges as a function of radiation pressure and mass ratio. The forbidden zone thicknesses have ranges because of the range of Jacobi constants that are allowed arising from the initial conditions ranging from $0.3R_{\rm H}$ to $0.5R_{\rm H}$.

APPENDIX C

Collisional Timescale of a Circumstellar Dust Grain

In this appendix, we calculate the collisional timescale t_{coll} of a circumstellar dust grain and show that this timescale is large compared to the disk lifetime, showing that collisions can generally be ignored since a dust grain is more likely to be accreted or ejected from the system than to undergo a collision. We start from the classic collisional timescale equation for a particle in a sea of similarly sized particles:

$$t_{coll} = \frac{1}{n\sigma v_{rel}} \tag{C.1}$$

where n is the number density of dust grains, σ is the cross-sectional area, and v_{rel} is the relative velocity between dust grains.

We calculate the number density by dividing the total number of grains in the system N by the volume of the space they occupy V. Specifically, we will calculate N by integrating over a collisional cascade size distribution and assume that 100% of dust grains exit the Hill sphere. Furthermore, we assume that the volume V is a toroidal volume with minor radius equal to the full width at half maximum (FWHM) measured in Figure 4.3 and major radius equal to the planet's semimajor axis plus the FWHM ($a + FWHM$). In other words, this is the toroidal space just outside of the forbidden zone of the restricted three-body problem where the thin ring is expected to be located. Since gravitational focussing is not important, the cross-sectional area is just the geometric cross section $\sigma = \pi(D/2)^2$. Lastly, we assume that v_{rel} will be on the order of the local Keplerian velocity $v_{kep} = (GM_*/a)^{1/2}$ of a circumstellar orbit.

C.1 Number of Dust Grains of a Given Size in a Collisional Cascade

In this section, we calculate the number of dust grains of a given size in a collisional cascade size distribution. We start by converting classical power law differential size distribution derived by Dohnanyi (1969) into the equation

$$\frac{dN}{dD} = AD^{-3.5}, \tag{C.2}$$

by introducing the normalization constant A. Since we need a finite interval to integrate over, we define a 'catastrophic collision' as one that occurs between two bodies that whose sizes are within a factor of 2. Thus, the number of similarly sized bodies that can catastrophically collide with a given body is

$$N = \int_0^N dN = \int_{D/2}^{2D} \frac{dN}{dD} dD = \int_{D/2}^{2D} AD^{-3.5} dD. \tag{C.3}$$

Evaluating this integral results in the following expression:

$$N = \frac{2}{5}\left(2^{5/2} - \frac{1}{2^{5/2}}\right)\frac{A}{D^{5/2}}. \tag{C.4}$$

Further evaluation of this expression is not possible without specifying the grain size of interest or normalizing the system as a whole. We will start by normalizing the system by total mass. The total mass M_{tot} of the collisional cascade can be obtained by integrating the differential size distribution over mass:

$$M_{tot} = \int_{D_{min}}^{D_{max}} m\frac{dN}{dD} dD, \tag{C.5}$$

where D_{min} is the minimum size body coupled to the collisional cascade, D_{max} is the maximum size body that initiates the cascade, and m is the mass of a given body. We will assume that the bodies are uniform density spheres, so $m = \rho(4\pi/3)(D/2)^3$. Will further assume that $D_{min} << D_{max}$. Evaluating this integral results in the following expression:

$$M_{tot} = A\rho\frac{\pi}{3}(D_{max}^{1/2} - \cancelto{0}{D_{min}^{1/2}}), \tag{C.6}$$

where D_{min} has been set to zero since it is assumed to be much smaller than D_{max}. We rearrange this expression to solve for the normalization constant A:

$$A = \frac{3}{\pi}\frac{M_{tot}}{\rho D_{max}^{1/2}}. \tag{C.7}$$

Combining Equations C.4 and C.7 results in a final expression for N:

$$N = \frac{6}{5\pi}\left(2^{5/2} - \frac{1}{2^{5/2}}\right)\frac{M_{tot}}{\rho D_{max}^{1/2} D^{5/2}}. \tag{C.8}$$

C.2 Collisional Timescale

We substitute all of the above described pieces into Equation C.1 to obtain the following analytic expression for the collisional timescale of a dust grain in a circumstellar orbit:

$$t_{coll} = \frac{40\pi^{1/2}3^{1/2}}{31}\frac{\rho^{1/2} D_{max}^{1/2} L_*^{1/2} \langle Q_{rad}\rangle^{1/2} a^{1/2} (FWHM)^2 (a + FWHM)}{G M_* c^{1/2} \beta^{1/2} M_{tot}}. \tag{C.9}$$

Plugging in reasonable values for the many open parameters results in the following expression:

$$\begin{aligned} t_{coll} = (4.75\ Myr)&\left(\frac{\rho}{1\ g/cm^3}\right)^{1/2}\left(\frac{\beta}{0.1}\right)^{-1/2}\left(\frac{D_{max}}{100\ km}\right)^{1/2}\left(\frac{M_{tot}}{0.001\ M_L}\right)^{-1}\left(\frac{M_*}{M_\odot}\right)^{-1} \\ &\times\left(\frac{L_*}{L_\odot}\right)^{1/2}\left(\frac{\langle Q_{rad}\rangle}{0.5}\right)^{1/2}\left(\frac{a}{a_J}\right)^{1/2}\left(\frac{FWHM}{0.9\ au}\right)^{2}\left(\frac{a + FWHM}{a_J + 0.9\ au}\right). \end{aligned} \tag{C.10}$$

This estimated collisional timescale represents a conservative lower limit for the following reasons:

1. The dust grains were assumed to occupy a narrow ~1 au torus just outside the forbidden zone, when in reality many of them are much further away as they spiral out of the system.

2. This calculation assumed that 100% of the dust grains escape from the Hill sphere and are present in the disk. In reality, over time the collisional timescale will increase as the number density decreases from dust grains being accreted or ejected from the system.

In any case, this collisional timescale is already much larger than even the largest disk lifetime in Table 6.2 (142,000 yr), thus showing that the average dust grain is more likely to be ejected from the system than collide with a similarly sized dust grain.

Bibliography

A. C. Boley, M. J. Payne, S. Corder, W. R. F. Dent, E. B. Ford, and M. Shabram. Constraining the Planetary System of Fomalhaut Using High-resolution ALMA Observations. , 750(1):L21, May 2012. doi: 10.1088/2041-8205/750/1/L21.

M. Bonnefoy, J. Milli, F. Menard, P. Delorme, A. Chomez, M. Bonavita, A-M. Lagrange, A. Vigan, J. C. Augereau, J. L. Beuzit, B. Biller, A. Boccaletti, G. Chauvin, S. Desidera, V. Faramaz, R. Galicher, R. Gratton, S. Hinkley, C. Lazzoni, E. Matthews, D. Mesa, C. Mordasini, D. Mouillet, J. Olofsson, and C. Pinte. Narrow belt of debris around the Sco-Cen star HD 141011. arXiv e-prints, art. arXiv:2111.03335, November 2021.

William F. Bottke, David Nesvorný, David Vokrouhlický, and Alessandro Morbidelli. The Irregular Satellites: The Most Collisionally Evolved Populations in the Solar System. , 139(3):994–1014, March 2010. doi: 10.1088/0004-6256/139/3/994.

J. A. Burns, P. L. Lamy, and S. Soter. Radiation forces on small particles in the solar system. , 40 (1):1–48, October 1979. doi: 10.1016/0019-1035(79)90050-2.

John Chambers. Mercury: A software package for orbital dynamics. Astrophysics Source Code Library, pages 01008–, 01 2012.

Christine Chen, Johan Mazoyer, Charles A. Poteet, Bin Ren, Gaspard Duchêne, Justin Hom, Pauline Arriaga, Maxwell A. Millar-Blanchaer, Jessica Arnold, Vanessa P. Bailey, Juan Sebastián Bruzzone, Jeffrey Chilcote, Élodie Choquet, Robert J. De Rosa, Zachary H. Draper, Thomas M. Esposito, Michael P. Fitzgerald, Katherine B. Follette, Pascale Hibon, Dean C. Hines, Paul Kalas, Franck Marchis, Brenda Matthews, Julien Milli, Jennifer Patience, Marshall D. Perrin, Laurent Pueyo, Abhijith Rajan, Fredrik T. Rantakyrö, Timothy J. Rodigas, Gael M. Roudier, Glenn Schneider, Rémi Soummer, Christopher Stark, Jason J. Wang, Kimberly Ward-Duong, Alycia J. Weinberger, David J. Wilner, and Schuyler Wolff. Multiband GPI Imaging of the HR 4796A Debris Disk. , 898(1):55, July 2020. doi: 10.3847/1538-4357/ab9aba.

E. Chiang, E. Kite, P. Kalas, J. R. Graham, and M. Clampin. Fomalhaut's Debris Disk and Planet: Constraining the Mass of Fomalhaut b from disk Morphology. , 693(1):734–749, March 2009. doi: 10.1088/0004-637X/693/1/734.

Thayne Currie, John Debes, Timothy J. Rodigas, Adam Burrows, Yoichi Itoh, Misato Fukagawa, Scott J. Kenyon, Marc Kuchner, and Soko Matsumura. Direct Imaging Confirmation and Characterization of a Dust-enshrouded Candidate Exoplanet Orbiting Fomalhaut. , 760(2):L32, December 2012. doi: 10.1088/2041-8205/760/2/L32.

J. S. Dohnanyi. Collisional Model of Asteroids and Their Debris. , 74:2531–2554, May 1969. doi: 10.1029/JB074i010p02531.

Raphaël Galicher, Christian Marois, B. Zuckerman, and Bruce Macintosh. Fomalhaut b: Independent Analysis of the Hubble Space Telescope Public Archive Data. , 769(1):42, May 2013. doi: 10.1088/0004-637X/769/1/42.

Peter Goldreich, Yoram Lithwick, and Re'em Sari. Final Stages of Planet Formation. , 614(1): 497–507, October 2004. doi: 10.1086/423612.

A. Meredith Hughes, Gaspard Duchêne, and Brenda C. Matthews. Debris Disks: Structure, Composition, and Variability. , 56:541–591, September 2018. doi: 10.1146/annurev-astro-081817-052035.

David Jewitt and Nader Haghighipour. Irregular Satellites of the Planets: Products of Capture in the Early Solar System. , 45(1):261–295, September 2007. doi: 10.1146/annurev.astro.44.051905.092459.

M. Jura. The Dust Debris around HR 4796. , 383:L79, December 1991. doi: 10.1086/186246.

Paul Kalas, James R. Graham, and Mark Clampin. A planetary system as the origin of structure in Fomalhaut's dust belt. , 435(7045):1067–1070, June 2005. doi: 10.1038/nature03601.

Paul Kalas, James R. Graham, Eugene Chiang, Michael P. Fitzgerald, Mark Clampin, Edwin S. Kite, Karl Stapelfeldt, Christian Marois, and John Krist. Optical Images of an Exosolar Planet 25 Light-Years from Earth. Science, 322(5906):1345, November 2008. doi: 10.1126/science.1166609.

Paul Kalas, James R. Graham, Michael P. Fitzgerald, and Mark Clampin. STIS Coronagraphic Imaging of Fomalhaut: Main Belt Structure and the Orbit of Fomalhaut b. , 775(1):56, September 2013. doi: 10.1088/0004-637X/775/1/56.

G. M. Kennedy and M. C. Wyatt. Collisional evolution of irregular satellite swarms: detectable dust around Solar system and extrasolar planets. , 412(4):2137–2153, April 2011. doi: 10.1111/j.1365-2966.2010.18041.x.

Scott J. Kenyon and Benjamin C. Bromley. Variations on Debris Disks III. Collisional Cascades and Giant Impacts in the Terrestrial Zones of Solar-type Stars. , 817(1):51, January 2016. doi: 10.3847/0004-637X/817/1/51.

Detlef Koschny and Eberhard Grün. Impacts into Ice-Silicate Mixtures: Ejecta Mass and Size Distributions. , 154(2):402–411, December 2001. doi: 10.1006/icar.2001.6708.

Alexander V. Krivov. Debris disks: seeing dust, thinking of planetesimals and planets. Research in Astronomy and Astrophysics, 10(5):383–414, May 2010. doi: 10.1088/1674-4527/10/5/001.

Eve J. Lee and Eugene Chiang. A Primer on Unifying Debris Disk Morphologies. , 827(2):125, August 2016. doi: 10.3847/0004-637X/827/2/125.

Mary Anne Limbach and Edwin L. Turner. Exoplanet orbital eccentricity: Multiplicity relation and the Solar System. Proceedings of the National Academy of Science, 112(1):20–24, January 2015. doi: 10.1073/pnas.1406545111.

Jack J. Lissauer. Planet formation. , 31:129–174, January 1993. doi: 10.1146/annurev.aa.31.090193.001021.

Xiaodong Liu and Jürgen Schmidt. Dust arcs in the region of Jupiter's Trojan asteroids. , 609:A57, January 2018. doi: 10.1051/0004-6361/201730951.

W. Lyra and M. Kuchner. Formation of sharp eccentric rings in debris disks with gas but without planets. , 499(7457):184–187, July 2013. doi: 10.1038/nature12281.

J. Milli, A. Vigan, D. Mouillet, A. M. Lagrange, J. C. Augereau, C. Pinte, D. Mawet, H. M. Schmid, A. Boccaletti, L. Matrà, Q. Kral, S. Ertel, G. Chauvin, A. Bazzon, F. Ménard, J. L. Beuzit, C. Thalmann, C. Dominik, M. Feldt, T. Henning, M. Min, J. H. Girard, R. Galicher, M. Bonnefoy, T. Fusco, J. de Boer, M. Janson, A. L. Maire, D. Mesa, J. E. Schlieder, and Sphere Consortium. Near-infrared scattered light properties of the HR 4796 A dust ring. A measured scattering phase function from 13.6° to 166.6°. , 599:A108, March 2017. doi: 10.1051/0004-6361/201527838.

C. D. Murray and S. F. Dermott. Solar system dynamics. 1999.

David Nesvorný, David Vokrouhlický, and Alessandro Morbidelli. Capture of Irregular Satellites during Planetary Encounters. , 133(5):1962–1976, May 2007. doi: 10.1086/512850.

J. Olofsson, J. Milli, P. Thébault, Q. Kral, F. Ménard, M. Janson, J. C. Augereau, A. Bayo, J. C. Beamín, Th. Henning, D. Iglesias, G. M. Kennedy, M. Montesinos, N. Pawellek, M. R. Schreiber, C. Zamora, M. Carbillet, P. Feautrier, T. Fusco, F. Madec, P. Rabou, A. Sevin, J. Szulágyi, and A. Zurlo. Dust production in the debris disk around HR 4796 A. , 630:A142, October 2019. doi: 10.1051/0004-6361/201935998.

Nicole Pawellek and Alexander V. Krivov. The dust grain size-stellar luminosity trend in debris discs. , 454(3):3207–3221, December 2015. doi: 10.1093/mnras/stv2142.

G. Schneider, A. J. Weinberger, E. E. Becklin, J. H. Debes, and B. A. Smith. STIS Imaging of the HR 4796A Circumstellar Debris Ring. , 137(1):53–61, January 2009. doi: 10.1088/0004-6256/137/1/53.

D. W. Schuerman. The restricted three-body problem including radiation pressure. , 238:337–342, May 1980. doi: 10.1086/157989.

M. C. Wyatt. Evolution of debris disks. , 46:339–383, September 2008. doi: 10.1146/annurev.astro.45.051806.110525.